Optimal Micro-Jet Flow Control for Compact Air Vehicle Inlets

Bernhard H. Anderson
Glenn Research Center, Cleveland, Ohio

Daniel N. Miller
Lockheed Martin Aerospace Company, Forth Worth, Texas

Gregory A. Addington
Wright-Patterson Air Force Base, Dayton, Ohio

Johan Agrell
Swedish Defence Research Agency, Bromma, Sweden

The NASA STI Program Office . . . in Profile

Since its founding, NASA has been dedicated to the advancement of aeronautics and space science. The NASA Scientific and Technical Information (STI) Program Office plays a key part in helping NASA maintain this important role.

The NASA STI Program Office is operated by Langley Research Center, the Lead Center for NASA's scientific and technical information. The NASA STI Program Office provides access to the NASA STI Database, the largest collection of aeronautical and space science STI in the world. The Program Office is also NASA's institutional mechanism for disseminating the results of its research and development activities. These results are published by NASA in the NASA STI Report Series, which includes the following report types:

- TECHNICAL PUBLICATION. Reports of completed research or a major significant phase of research that present the results of NASA programs and include extensive data or theoretical analysis. Includes compilations of significant scientific and technical data and information deemed to be of continuing reference value. NASA's counterpart of peer-reviewed formal professional papers but has less stringent limitations on manuscript length and extent of graphic presentations.

- TECHNICAL MEMORANDUM. Scientific and technical findings that are preliminary or of specialized interest, e.g., quick release reports, working papers, and bibliographies that contain minimal annotation. Does not contain extensive analysis.

- CONTRACTOR REPORT. Scientific and technical findings by NASA-sponsored contractors and grantees.

- CONFERENCE PUBLICATION. Collected papers from scientific and technical conferences, symposia, seminars, or other meetings sponsored or cosponsored by NASA.

- SPECIAL PUBLICATION. Scientific, technical, or historical information from NASA programs, projects, and missions, often concerned with subjects having substantial public interest.

- TECHNICAL TRANSLATION. English-language translations of foreign scientific and technical material pertinent to NASA's mission.

Specialized services that complement the STI Program Office's diverse offerings include creating custom thesauri, building customized databases, organizing and publishing research results . . . even providing videos.

For more information about the NASA STI Program Office, see the following:

- Access the NASA STI Program Home Page at *http://www.sti.nasa.gov*

- E-mail your question via the Internet to help@sti.nasa.gov

- Fax your question to the NASA Access Help Desk at 301–621–0134

- Telephone the NASA Access Help Desk at 301–621–0390

- Write to:
  NASA Access Help Desk
  NASA Center for AeroSpace Information
  7121 Standard Drive
  Hanover, MD 21076
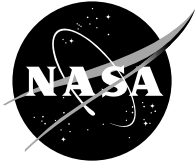
Optimal Micro-Jet Flow Control for Compact Air Vehicle Inlets

Bernhard H. Anderson
Glenn Research Center, Cleveland, Ohio

Daniel N. Miller
Lockheed Martin Aerospace Company, Forth Worth, Texas

Gregory A. Addington
Wright-Patterson Air Force Base, Dayton, Ohio

Johan Agrell
Swedish Defence Research Agency, Bromma, Sweden

National Aeronautics and
Space Administration

Glenn Research Center

February 2004

Available from

OPTIMAL MICRO-JET FLOW CONTROL FOR COMPACT
AIR VEHICLE INLETS

Bernhard H. Anderson
National Aeronautics and Space Administration
Glenn Research Center
Cleveland, Ohio 44135

Daniel N. Miller
Lockheed Martin Aerospace Company
Fort Worth, Texas 76101

Gregory A. Addington
Wright-Patterson Air Force Base
Dayton, Ohio 45433

Johan Agrell
Swedish Defence Research Agency
Bromma, Sweden SE–17290

ABSTRACT

The purpose of this study on micro-jet secondary flow control is to demonstrate the viability and economy of *Response Surface Methodology* (RSM) to optimally design micro-jet secondary flow control arrays, and to establish that the aeromechanical effects of engine face distortion can also be included in the design and optimization process. These statistical design concepts were used to investigate the design characteristics of "low mass" micro-jet array designs. The term "low mass" micro-jet array refers to fluidic jets with total (integrated) mass flow ratios between 0.10% and 1.0% of the engine face mass flow. Therefore, this report examines optimal micro-jet array designs for compact inlets through a *Response Surface Methodology*.

INTRODUCTION

The current development strategy for combat air-vehicles is directed towards reduction in the Life-Cycle Cost (LCC) with little or no compromise to air-vehicle performance and survivability. This strategy has been extended to the aircraft component level, in particular, the engine inlet diffuser system. One method to reduce inlet system LCC is to reduce its structural weight and volume. Consequently, advanced combat inlet configurations are being made more compact (or shorter) to achieve weight and volume (and LCC) reduction. However, compact S-duct diffusers are characterized by high distortion and low pressure recovery, which are produced by extreme wall curvature and strong secondary flow gradients. These characteristics are further aggravated by maneuvering conditions. The requirement to highly integrate or embed the propulsion system often leads to conformal inlet aperture shapes which do not lend themselves to good aerodynamic performance. These configurations also present a challenging environment for both fan/compressor surge margin and aeromechanical vibration. Interest in High Cycle Fatigue (HCF) research by the US aerospace community has been spurred by discrepancies between the expected durability of engine components compared to that actually experienced in the field. Recognizing that inlet distortion is a forcing function for vibration in the fan components, methods for increasing HCF Life Expectancy can be combined with techniques for inlet recovery and engine face distortion management. Therefore, to enable acceptable performance levels in such advanced,

compact inlet diffuser configurations, micro-scale secondary flow control (MSFC) methods are being developed to manage the recovery, distortion, and HCF aspects of distortion.[1]-[2]

One of the most difficult tasks in the design of micro-scale arrays for optimal inlet operation is arriving at the geometric placement, arrangement, number, size and orientation of the effector devices within the inlet duct to achieve optimal performance. These effector devices can be activated by either mechanical or fluidic means. This task is complicated not only by the large number of possible design variables available to the aerodynamicist, but also by the number of decisions parameters that are brought into the design process. By including the HCF effects into the inlet design process, the aerodynamicist has a total of seven individual response variables which measure various aspect of inlet performance. They include the inlet total pressure recovery, the inlet total pressure recovery distortion at the engine face and the first five Fourier harmonic 1/2 amplitudes of distortion. Each of these responses needs to be either maximized, minimized, constrained or unconstrained while searching for the optimal combination of primary design variable values that satisfy the mission requirements. The design task is further complicated by the existence of hard-to-control factors which affect inlet performance, i.e. the mission variables. The design of inlet systems is usually accomplished at the cruise condition (the on-design condition) while variations from the cruise condition are considered as an off-design penalty. The mission variables that cause the off-design penalty are, for example, inlet throat Mach number (engine corrected weight flow), angle-of-incidence and angle-of-yaw. Numerical optimization procedures that have been successful with some aerodynamic problems give little assistance to the design of micro-scale secondary flow arrays. It is very difficult to incorporate large numbers of independent design and response variables into such procedures. Further, they are very expensive to use if the individual Computational Fluid Dynamics (CFD) experiments are solutions to the full Navier-Stokes equations in three dimensions. However, there is a statistical approach to the problem which combines an optimally sequenced pattern of Design-of-Experiments (DOE), statistical model building, and system optimization called *Response Surface Methodology* (RSM). It is ideally suited to the design of micro-jet arrays for optimal inlet performance, particularly when multiple design objectives are present.

In the 1950s and 1960s, Box[3]-[4] and co-workers developed a collection of analytical and statistical experimental design tools for which the term *Response Surface Methodology* (RSM) was coined. RSM provides an economical, reliable and systematic approach to variable screening as well as the general exploration of the region that contains the estimated optimal conditions. As a result, the pragmatic use of RSM places a high priority on obtaining a better understanding of the process system as well as estimating the optimum conditions. In the design of micro-scale secondary flow arrays for inlets, it is just as important to understand and quantify the behavior of the design parameters in the neighborhood of the optimal conditions as to know the optimal conditions. Hence, an RSM approach is particularly beneficial for the design of micro-jet arrays since there are a great many design variables available to the aerodynamicist, and often there exist multiple design objectives. Another critical aspect of RSM is its ability to study statistical interactions among the design variables. These interactions often indicate a potential for achieving a robust control factor combination. A robust control factor combination is one for which variations in the individual factors has minimal effect on the response variables. The robustness increases as the tolerable variation in the design factors increases.

A statistical interaction exists between two independent factor variables X1 and X2 when the effect of X1 on response Yi is affected by the value of X2. In other words, the effect

of factor X1 on response Yi is not unique, but changes as a function of factor X2. This is often called a synergistic effect, and it is very important in micro-jet array design. In addition, it is often desirable in inlet design to satisfy several objectives at one time. For example, in designing an inlet for HCF considerations, it may be desirable to determine the combination of factor settings that maximize inlet total pressure recovery, minimize engine face distortion, and constrain a particular Fourier harmonic 1/2 amplitude of distortion to a given safe value at the natural resonance frequency of the engine fan blades. However, since the resonance frequency of the engine blades is not generally known, the desired design goal may be to collectively reduce all the Fourier harmonic 1/2 amplitudes of engine face distortion.

In this research study on micro-jet flow control, three objectives were considered important, namely: (1) to determine the design characteristics of micro-jet secondary flow control arrays, (2) to establish the ability of micro-jet arrays to manage the aeromechanical effects of engine face distortion, and (3) to evaluate the effectiveness of robust parameter design methodologies for high performance "open loop" micro-jet arrays designs over a range of throat Mach numbers and angle-of-incidences. This report covers the first two research objectives while Anderson, Miller, Addington, and Agrell[5] cover the third objective and describe a design methodology whereby the hard-to-control mission variables are explicitly included in the design of optimal robust micro-jet arrays.

NOMENCLATURE

AIP	Aerodynamic Interface Plane
Ap	Micro-Jet Pitch Angle
As	Micro-Jet Skew Angle
c	Effector Chord Length
CCF	Central Composite Face-Centered
CFD	Computational Fluid Dynamics
D	Engine Face Diameter
DC60	Circumferential Distortion Descriptor
DOE	Design of Experiments
Djet	Diameter of Micro-Jet
Fk/2	k^{th} Fourier Harmonic 1/2-Amplitude
FM/2	Mean Fourier Harmonic 1/2-Amplitude
h	Effector Blade Height
HCF	High Cycle Fatigue
Kbnd	Number of Micro-jet Effector Bands
Kjet	Number of Micro-Jet Effectors per. Band
L	Inlet Diffuser Length
LCC	Life Cycle Costs
MSFC	Micro-Scale Secondary Flow Control
Mt	Inlet Throat Mach Number
Njet	Total Number of Micro-Jet Effectors
n	Number of Effector Vanes per Band
Pjet	Micro-jet Total pressure
PFAVE	Average Inlet Total Pressure at AIP
PAVCRIT	Minimum Total Pressure over Critical Sector Angle at AIP

Pt	Total Pressure
QAVE	Average Dynamic Pressure at AIP
R	Inlet Radius
R_{cl}	Centerline Radius
R_{ef}	Engine Face Radius
R_{thr}	Inlet Throat Radius
ROC	Robust Optimization Concepts
Rey	Reynold Number per ft.
RSM	Response Surface Methodology
S	Standard Deviation
S_{clock}	Standard Deviation over the Rake Clocking Angles
Tt	Total temperature
UAV	Unmanned Air Vehicle
UCAV	Unmanned Combact Air Vehicle
Waip	AIP or Engine Face Mass Flow
Wjet	Total Jet Mass Flow
wjet	Individual Jet Effector Mass Flow
X_{cl}	Axial Distance Along the Duct Centerline
Y_A	Upper 95% Confidence Interval Predicted by DOE Analysis
Y_{CFD}	Response Predicted by CFD Analysis
Y_{DOE}	Response Predicted by DOE Analysis
$Y_{i,j}$	Generalized Response Variable
$Y_{M,\alpha}$	Generalized Response Variable Summed over Mt and α
Z_{cl}	Centerline Offset Displacement
α	Inlet Angle-of-Incidence
β	Effector Vane Angle-of-Incidence
ΔZ_{cl}	1/2 Inlet Centerline Offset
γ	Inlet Angle-of-Yaw

RESULTS AND DISCUSSION

Baseline Flow in the Redesigned M2129 Inlet S-Duct

The redsigned M2129 inlet S-duct used in this study was considered similar to the original DERA/M2129 inlet S-duct defined by AGARD FDP Working Group 13 Test Case 3,[6] using Lip No. 3 and Forward Extension No. 2. This inlet design was first proposed by Willmer, Brown and Goldsmith,[7] and has been used extensively in the US and UK to explore inlet flow control array design. The centerline for the redesigned M2129 inlet is given by the equation

$$Z_{cl} = -\frac{\Delta Z_{cl}}{2}\left(1 - \cos\left(\pi \cdot \frac{X_{cl}}{L}\right)\right) \quad (1)$$

the radius distribution measured normal to the inlet centerline is given by the expression

$$\left(\frac{R_{cl} - R_{thr}}{R_{ef} - R_{thr}}\right) = 3\left(1 - \frac{X_{cl}}{L}\right)^4 - 4\left(1 - \frac{X_{cl}}{L}\right)^3 + 1 \quad (2)$$

where $R_{thr} = 2.5355$ inches, $R_{ef} = 3.0$ inches, $L = 15.0$ inches, and $\Delta Z_{cl} = 5.7809$ inches. The redesign of the M2129 inlet is such that the new inlet matches the static pressure gradients normally found in typical UAV or UCAV designs. Therefore, the new inlet is more compact than the original M2129 inlet S-duct. As a consequence, supersonic flow will develop in this inlet when the inlet throat Mach number increases much above 0.70. The geometry and grid structure for the resigned M2129 inlet S-duct is described in detail in Anderson, Baust, and Agrell.[5].

Traditionally, this type of compact inlet duct would be excluded from design consideration since it is characterized by severe wall curvature that induces strong secondary flows. These strong secondary flow can cause a flow separation called vortex lift-off. See Figure (1). This type of 3D flow separation results in severe total pressure losses and engine face distortion. Figure (2) presents the engine face total pressure recovery contours and secondary flow velocity vectors for the redesigned DERA/M2129 inlet S-duct at a throat Mach number of 0.70. A vortex pair is the dominant flow field in the engine face flow field and this is accompanied by very severe engine face total pressure distortion.

Inlet Flow Control Micro-Jet Effector Design Approach

If an air-jet is issued into a cross flow, a high pressure region will be formed at the front of the jet and a low pressure wake will form in the rear. Since the jet passes perpendicular to to free stream, some stream flow will be entrained into the jet, and separation of the cross flow around the jet will be drawn away forming a pair of counter rotating vortices downstream. For the air-jet issuing through the boundary layer, the separation of the boundary layer before the jet will cause the same effect with the added vorticity from the boundary layer added to the vortex core. There have been extensive studies on the flow physics of an steady state air-jet issuing into a cross flow, and these have been carefully cataloged in a Ph'D thesis by Bray.[8]

In 1994, Gibb and Jackson[9-10] demonstrated that air-jet generators can successfully control the flow in a high speed inlet. By pitching the jet at an angle to the surface, and yawing the jet from the free stream, a difference in strength of the counter rotating vortices would result. One of these vortices will become stronger, while the other will become weaker. Often, the weaker vortex will dampen out. Further investigation by Bray, Weir, and Gibb[11] have also shown that the vortices induced by air-jets controlled separation within high speed inlets in a manner similar to vanes. Thus, air-jet actuation was used as an approach called "secondary flow control" to alter the inlet S-duct inherent secondary flow with the goal of simultaneously improving the critical system level performance metrics. While it has been shown that air-jets manage flow in an inlet in a similar manner to vanes, the structure of the air-jet vortices were radically different from those produced by vanes.[8]

While there is a wealth of experimental data on the characteristics of a single jet issuing into a free stream, a problem exists because there is little information on the behavior of a cascade or an array of jets issuing through a boundary layer into a core flow. Both micro-vanes and air-jet inlet flow control arrays are designed as a cascade or an array of effectors. Conse-

quently, the effectors within the array interact with each other. A micro-vane or air-jet within an array behaves very differently than an isolated effector. For example, a micro-vane in an array (or cascade) can be set at a much higher angle-of-incidence than an isolated vane and still operate very effectively.

A second major problem associated with the design of air-jet flow control within inlets are the factor (design) parameters themselves. The factor (design) parameters for air-jet generators have been identified[8] and include the jet pitch angle, jet skew angle, jet hole diameter, and jet Mach number ratio or jet momentum ratio. While the jet Mach number or momentum ratio is useful, it is the total or integrated mass flow that is that is the critical design parameter. A heavy performance penalty is paid by bleeding flow from the engine or acquiring the flow from some other source. Therefore it is essential that engine bleed flow ratio (Wjet/Waip) be an inlet design factor. The term "low mass" or micro-jet effector arrays used in this report will refer to fluidic jets with total (integrated) mass flows between 0.10% and 1.0% of the engine face mass flow (Waip).

A third major problem associated with the design micro-jet flow control within inlets is the response variables themselves. The peak vorticity production has been identified in many studies[9] as the response parameter used to measure the performance of the micro-jet effectors. However, it is the effectiveness of vorticity production in managing engine face distortion, as measured in terms of a distortion descriptor, that most concerns inlet designers. However, there is no correlation between generating vorticity using micro-jets and managing engine face distortion using micro-jet effectors. For example, a micro-jet effector array can generate a great deal of vorticity. However, if that vorticity is not properly located and positioned within the inlet flow field, it will not be very effective in managing inlet distortion. Hence the lack of correlation between generating vorticity and managing engine face distortion.

Effective inlet flow control management of engine face distortion was achieved using micro-vane arrays by reducing the unit strength of the vane effectors and allowing the array design to influence the inlet flow over an extended streamwise distance. With this combination, the total pressure losses associated with micro-vane effectors became very small, and a large overall gain in managing both inlet total pressure recovery and engine face distortion was achieved.[12] Likewise, it could be expected that an overall gain in managing inlet total pressure recovery and engine face distortion is possible by using micro-jet array designs that influence the near wall inlet flow over an extended streamwise distance. This was examined in this study by considering multiple bands of micro-jet effectors (Kbnd) and multiple number of micro-jets per band (Kjet) in the factor space. With this factor construction, the individual micro-jet mass flow ratio (wjet/Waip) varied from 0.001% to 0.10%.

Inlet Flow Control Micro-Jet Effector Array Design

To manage the flow in the redesigned M2129 inlet S-duct, a multi-band array arrangement of micro-jet effectors was placed in the upstream section near the inlet throat. See Figures (3). The location of the individual bands are shown in Figure (3a) for a single band array, Figure (3b) for as three band array, and in Figure (3c) for a five band micro-jet array. The dimensions shown were measured in the axial direction along the S-duct centerline from the inlet throat station to the intersection of the appropriate cross-sectional plane and the S-duct centerline. In each of the band arrangements shown in Figure (3), the configuration was considered to represent

the approximate streamwise distance associated with the optimal micro-vane effector chord length in Anderson, Baust, and Agrell[12], or about 72 mm.

The DOE approach followed directly from the objectives previously stated and was reflected in the layout of the design factors listed in Table (1). The factor variables were the number of micro-jet effector bands (Kbnd), the number of micro-jet effectors per band (Kjet), the micro-jet pitch angle (Ap), the micro-jet skew angle (As), and the percent total or integrated micro-jet mass flow ratio, i.e.

$$\frac{\text{Wjet}}{\text{Waip}} = 100.0 \sum_{i=1}^{\text{Njet}} \left(\frac{\text{wjet}}{\text{Waip}} \right)_i \quad (3)$$

here $\left(\dfrac{\text{wjet}}{\text{Waip}} \right)_i$ is the individual micro-jet effector mass flow ratio, and Njet is the total number of micro jets in the array, i.e. $\text{Njet} = \text{Kbnd} \cdot \text{Kjet}$. The micro-jet hole diameter Djet was sized such that the appropriate percent jet total mass flow ratio $\dfrac{\text{Wjet}}{\text{Waip}}$ was established at a jet total pressure (Pjet) of three (3) bar. The definition of the micro-jet pitch angle (Ap) and micro-jet skew angle (As) is illustrated schematically in Figures (4) and (5) respectively. Table (2) shows the variables that were held constant during this study. They include the inlet throat Mach number (Mt), the inlet operating total pressure (Pt) and temperature (Tt), the inlet Reynolds number (Rey), and the micro-jet total pressure (Pjet). Table (3) displays the response variables for this study. They include the inlet total pressure recovery (PFAVE), the engine face distortion (DC60), and the first five Fourier harmonic 1/2-amplitudes of engine face distortion (F1/2, F2/2, F3/2, F4/2, and F5/2)

The DOE strategy selected was a Central Composite Face-Centered (CCF) DOE. This strategy resulted in 27 unique CFD experimental cases that are shown in Table (4).This particular DOE, like most DOE strategies, varied more than one factor at a time. Further, this layout of 27 cases permitted the estimation of both linear and curvilinear effects as well as two-factor interactive or synergistic effects among the DOE factors. This CCF DOE strategy is superior to the traditional approach of changing one variable at a time because this does not permit the estimation of the two-factor interactions. The 27 runs of the CCF DOE is also more economical than a full factorial approach where the number of experiments would be 3^5 or 243 separate cases.

A graphical representation of the Central Composite Face-Centered DOE used in the study is presented in Figure (6). The DOE cases are represented in this figure by the circular symbols, where the symbol locations on the cube signify the factor values. This DOE is called a composite DOE because the cases are composed of a fractional factorial part and a quadratic part. The fractional factorial part of the DOE is composed of one-half of the 2^5 possible cases, i.e. 32 possible factorial cases, which are represented by the eight corner locations in each of the four corner-cubes in Figure (6). Because only half the number of possible factorial cases are actually used in this DOE format (circular symbols), the layout is called a 1/2-fractional of the full factorial and is composed of 2^{5-1} cases, or 16 separate CFD runs. The remaining cases in Figure (6) are the quadratic part of the DOE. These cases allow for the evaluation of the linear and curvilinear effects. All together, there are a total of 27 cases in a Central Composite Face-Centered DOE with five factor variables. Notice the balanced layout of cases in Figure (6). The factor variables are

represented by the axes of the individual cubes, while the environmental variables are represented by the different cubes. This layout of cases represents the smallest number of CCF DOE cases that allows for the evaluation of linear and curvilinear effects as well as all two-factor interactive or synergistic effects.

Each of the 27 cases in Table (4) was run with a Reynolds-averaged Navier-Stokes code[13] that allowed for numerical simulation of both micro-vane or micro-jet effectors without the need to physically embed the vanes or jets effectors within the CFD grid structure.The half cylindrical grid structure was composed of three blocks: an upstream block, an effector section containing the micro-vanes, and a downstream block. The computational half-plane grid structure contained 945,553 grid points. All CFD calculations were accomplished assuming half cylindrical symmetry. A two-equation k-l turbulence model was used in this study. This model consists of a transport equation for the turbulent kinetic energy and turbulent length scale. The model also includes a near-wall model and compressible corrections for high speed flows.

Harmonic Analysis of Distortion

The overall methodology used to obtain the harmonic content of inlet distortion was first proposed by Ludwig[14]. This methodology is characterized by the use of radial weighting factors applied to the total pressure rake measurements. The radial weighting factors are shown in Table (5). These radial weighting factors compress the rake information to a single radius ring of data samples, where the number of data samples corresponds to the number of arms of the measurement rake. A separate study was initiated by Anderson and Keller[15] to evaluate the impact of rake geometry (specifically the number of rake arms) on the measurement error associated with estimating the first five Fourier harmonic 1/2-amplitudes of engine face distortion. As a result of that study, the rake and methodology chosen for this study was the 80-probe "clocked" AIP rake because it provided the lowest error in estimating the first five Fourier harmonic 1/2-amplitudes of engine face distortion. Clocking the AIP rake means that N separate measurements were taken, and at each separate measurement, the angular orientation of the rake was advanced by an amount 1/N times the rake angle. The rake angle is the ratio of 360° divided by the number of arms in the AIP rake. For example, a standard 80-probe rake has 16-arms. Hence the rake angle is 22.5^o. Therefore total pressure measurements were obtained at each $22.5^o/N$ angular position of the rake. Using the AIP instrumentation locations for the 80-probe rake, the 27 CFD solutions were interpolated at each of the probe positions shown in Figure (7a). The span-weighted average total pressure was calculated for the 80-probe rake by multiplying the probe total pressure by the span-weighted coefficients from Table (5), and adding the results over the five probes of the rakes to form a single radius ring of data samples.

Since the rake at the engine face was "clocked", a complete set of "repeats" was generated at each experimental run in Table (4). From the engine face patterns at each of the 10 clocking angles, a Fourier analysis was performed on the sample set of data and a standard deviation of the "repeats", S_{clock}, was determined for each of the Fourier harmonic 1/2-amplitudes. In order to check the constant variance assumption associated with least square regression, a simple F-test for comparing the minimum standard deviation to the maximum standard deviation ($F = S^2_{max}/S^2_{min}$) was conducted for each of the five responses. The results are presented in Table (6). Since each F-test exceeded the 95% confidence critical value of $F(0.975,9,9) = 4.03$, the assump-

tion of constant variance across the design space had to be discarded. This meant that a regression technique known as weighted least squares regression had to be employed for analyzing the 10 x 27 = 270 data samples in the DOE. The weights in these regression analyses were set to $1/S^2_{clock}$.

The data reduction for the inlet total pressure recovery and engine face distortion differed greatly from the harmonic analysis of distortion described. There exists no recognized methodology to evaluate the Fourier harmonic 1/2-amplitudes of engine face distortion for more than five probes in the radial direction. Hence, evaluating the Fourier harmonic 1/2-amplitude directly from the computational mesh had to be discarded. However, both the inlet total pressure recovery and engine face distortion can and were calculated directly from the computational grid at the engine face station. This computational mesh was composed of 49 x 121 grid points in the full-plane. The DC60 engine face distortion descriptor is defined such that it can be determined from either a computational grid or a standard measurement rake.[16] It is the only recognized distortion descriptor that has this property, and hence, was chosen for this study. The DC60 engine face distortion descriptor is a measure of the difference between the engine face or AIP average total pressure (PFAVE) and the lowest average total pressure in any sector defined by a critical angle of 60° (PAVCRIT), divided by the average dynamic pressure at the engine (AIP) face. Hence,

$$DC60 = \frac{(PFAVE - PAVCRIT)}{QAVE} \quad (4)$$

The CFD performance results for the Central Composite Face-Centered DOE format involving the factor (design) variables are presented in Table (7). The inlet recovery (PFAVE) and the engine face distortion (DC60) were determined from the computation mesh. The Fourier harmonics 1/2-amplitudes of engine face distortion listed in Table (7) were determined from a "clocked" engine face rake and are the mean values over the 10 clocking angles. However, these values were not used in the regression analysis since weighted regression were required as a result of a lack of constant variance across the design space. Instead, the complete set of 10 x 27 = 270 values together with their corresponding weighting factors were used in the weighted regression to obtain the response surfaces for each of the Fourier harmonic 1/2-amplitudes of distortion. The engine face total pressure recovery contours for the Central Composite Face-Centered DOE shown in Table (4) is presented in Figure (8).

Interactions Between the Factor Variables

The significant terms in the DOE regression model for inlet total pressure recovery (PFAVE) are shown in Table (8), while the significant terms in the DOE regression model for the engine face distortion (DC60) are shown in Table (9). There were two important two-way factor factor interactions identified for inlet total pressure recovery regression model and one important two-way factor interactions identified for the DC60 distortion regression model. See Tables (8) and (9). For inlet total pressure recovery, the (Ap*Wjet/Waip) and (As*Wjet/Waip) were identified as significant, while the (As*Wjet/Waip) two-way interaction was revealed to be important for the engine face distortion regression model. The significance p-values listed on Tables (8) and (9) are the defined as the probability of observing an absolute t-value that is greater than one calculated when there is no effect present. The regression models listed in Tables (8) and (9) were

obtained from a backward elimination. Backwards elimination begins with the full model and deletes or eliminates the least significant term in the model until all terms left in the model are statistically significant. In the models listed in Tables (8) and (9), all terms with a significant level $p \leq 0.20$ were retained. The relationship between p and % Signif is given by the expression:

$$\% \text{ Signif} = 100.0(1.0 - p) \qquad (4)$$

Therefore, the DOE regression model only includes terms that are statistically significant.

A statistical interaction exists between two independent factor variables X1 and X2 when the effect of X1 on response Yi is affected by the value of X2. In other words, the effect of factor X1 on response Yi is not unique, but changes as a function factor X2. For example, Figure (9) presents the inlet performance metrics PFAVE as a function of the total jet mass flow ratio (Wjet/Waip) at three levels of the pitch angle (Ap). However, the rate of increase of PFAVE as a function of total jet mass flow ratio (Wjet/Waip) depends on the pitch angle (Ap). See Figure (10). The (Ap*Wjet/Waip) interaction indicates that the optimal jet pitch angle (Ap) will depend on the total jet mass flow ratio (Wjet/Waip) selected for the micro-jet array design.

A statistical interaction can also be understood by illustrating a functional relationship that does not reflect a synergistic effect between two factor variables. Presented in Figure (10) is the inlet performance metric (PFAVE) as a function of the total jet mass flow ratio (Wjet/Waip) at three levels of the number of micro-jets per band, i.e. the factor Kjet. Since the relationship between (PFAVE) and (Wjet/Waip) differ only by an additive constant at the three levels of Kjet, there is no (Kjet*Wjet/Waip) statistical interaction. This is substantiated in Table (8) which list the significant regression terms for the inlet total pressure recovery (PFAVE). Thus, the optimal number of micro-jets per band (Kjet) will not depend on the total jet mass flow ratio (Wjet/Waip) selected for the micro-jet array design.

Figures (11) and (12) illustrate the (As*Wjet/Waip) statistical interactions that were designated as being statistically significant in Tables (8) and (9) for the inlet total pressure recovery characteristics (PFAVE) and engine face distortion (DC60). In each case, the rate of change of the response variables (PFAVE) and (DC60) with total jet mass flow ratio (Wjet/Waip) depended on the micro-jet skew angle (As). Consequently, the optimal jet skew angle (As) will depend on the total jet mass flow ratio (Wjet/Waip) selected for the micro-jet array design.

Optimal Flow Control for Three Missions

To illustrate the potential of *RSM* to select an optimal micro-jet array design, three mission strategies were considered for the subject inlet, namely (1) Maximum Performance, (2) Maximum Engine Stability, and (3) Maximum HCF Life Expectancy. The Maximum Performance mission minimized the inlet total pressure losses, the Maximum Engine Stability mission minimized the engine face distortion, while the Maximum HCF Life Expectancy mission minimized the mean of the first five Fourier harmonic amplitudes, i.e. "collectively" reduced all the harmonic 1/2-amplitudes of engine face distortion. Each of the mission strategies was subject to a low engine face distortion constraint, i.e. DC60 < 0.10, which is a level acceptable for commercial engines, and a constraint on each individual Fourier harmonic 1/2-amplitudes: Fk/2 < 0.015, k = 1,2...5.

Maximum Performance Mission - To obtain the Optimal Maximum Performance array design, a search was made of the factor design space to locate that factor combination the minimized the inlet duct losses:

$$Y = (1.0 - PFAVE) \quad (5)$$

subject to the constant that

$$DC60 \leq 0.01 \quad (6)$$

and the individual Fourier harmonic 1/2-amplitudes of engine face distortion were each constrained to

$$\frac{Fk}{2} \leq 0.015 \quad (7)$$

Maximum Engine Stability Mission - In a like manner, the Optimal Maximum Engine Stability array design was obtained through a search process over the factor design space to locate that factor combination that minimized decision parameter:

$$Y = (DC60) \quad (8)$$

subject to the condition that the individual Fourier harmonic 1/2-amplitudes of engine face distortion were each constrained to

$$\frac{Fk}{2} \leq 0.015 \quad (9)$$

while the total pressure recovery (PFAVE) was unconstrained.
.   **Maximum HCF Life Expectancy Mission** -The Optimal Maximum HCF Life Expectancy MSFC array was determined through a search process over the factor variable space to locate that array geometry that minimized the mean of the first five Fourier harmonic 1/2-amplitudes of distortion, i.e

$$Y = \frac{1}{5} \sum_{k=1}^{5} \left(\frac{Fk}{2} \right) \quad (10)$$

subject to the constant that

$$DC60 \leq 0.01 \quad (11)$$

and that the individual Fourier harmonic 1/2-amplitudes of engine face distortion were each constrained to

$$\frac{\text{Fk}}{2} \le 0.015 \quad (12)$$

while the total pressure recovery (PFAVE) was unconstrained in the search procedure.

Comparison of the Optimal Array Designs

Presented in Table (10) are the results of the search process over the factor design space for the three missions, i.e. the Maximum Performance, the Maximum Engine Stability, and the Maximum HCF Life expectancy, to arrive at the optimal array designs as predicted by the DOE regression model. A series of three CFD validation cases listed in Table (10) were run using the optimal factor combinations determined from the DOE regression model. The CFD engine face performance results are presented in Table (11). Therefore, Tables (10) and (11) present the optimal engine face performance results for each of the three missions as determined from the DOE predictions and by the CFD analyses. Eight response variables are listed in Tables (10) and (11). They include the inlet total pressure (PFAVE), the engine face distortion (DC60), and the first five Fourier harmonic 1/2 amplitudes of distortion (F1/2, F2/2, F3/2, F4/2, F5/2). The mean of the first five Fourier harmonic 1/2 amplitudes of distortion (FM/2) was determined from the expression:

$$\frac{\text{FM}}{2} = \frac{1}{5} \sum_{k=1}^{5} \left(\frac{\text{Fk}}{2} \right) \quad (13)$$

Comparison of the performance of the three "Optimal Robust" array designs, i.e. the Maximum Performance, Maximum Engine Stability, and Maximum HCF Life Expectancy mission designs listed in Table (10) and (11) indicates that performance of the three optimal array designs are remarkably similar. It is also true that the performance predicted by the DOE regression is also remarkably similar to the CFD analysis for each of the missions. This visual similarity will be studied objectively in the section entitled "Statistical Comparison of the CFD Analysis and DOE Predictions".

Figure (13) presents a comparison of the engine face total pressure recovery contours and secondary flow field for each of the validation solutions obtained from the CFD analysis. Although the three "Optimal Robust" array designs were generated from three very different mission strategies, the engine face flow field achieved by these array designs were visually not significantly different. Figures (14) through (16) illustrates the near wall streamlines for the three optimal array designs. Shown in these figures are both the near wall streamline lines for the entire inlet as well as an enlarged image of the effector region near wall streamline lines.

Comparison of Optimal Micro-Vane and Optimal Micro-Jet Designs

Comparison of the performance of the three "Optimal Robust" array designs, i.e. the Maximum Performance, Maximum Engine Stability, and Maximum HCF Life Expectancy mission designs, are shown in Figures (17) through (19) for both the set of three optimal micro-vane designs and the set of three optimal micro-jet array designs. Optimal micro-jet arrays were

examined in Anderson, Miller, Addington, and Agrell[5] and the summary performance presented in this report for comparison with the optimal micro-vane designs. These figures also include the baseline inlet performance, i.e. the performance of the redsigned M2129 inlet S-duct without flow control. The low strength effector units used in these designs achieved a substantial improvement in inlet total pressure recovery (PFAVE) over the baseline performance. See Figure (17). This differs from the performance of the high strength effector units which never increased the inlet total pressure recovery above the baseline value[4]. A comparison between the set of three (3) optimal micro-jet arrays and the set of three (3) optimal micro-vane arrays indicates a substantial increase in total pressure recovery as a result of the using micro-jet arrays. See Figures (17a) and (17b). However, care must be taken in making judgements about micro-jets vs. micro-vane as the penalty for bleeding 1.0% engine flow has not been included in this study.

Excellent engine face distortion characteristics were also achieved with the micro-effector units, i.e both micro-jet and micro-vanes, as shown in Figure (18). Essentially no performance differences were evident between micro-vanes and micro-jet arrays with regards to engine face distortion. See Figures (18a) and (18b).

Presented in Figure (19) is a comparison of the first five Fourier harmonic 1/2-amplitudes for the set of three (3) optimal designs for both micro-jet and micro-vane arrays. Minimizing the mean of the first five Fourier harmonic 1/2-amplitudes resulted in a substantial reduction in the amplitudes of the first three harmonics 1/2-amplitudes, and very low amplitudes for the fourth and fifth harmonic components. Figures (19a) and (19b) include eighteen (18) matched pairs of independent CFD observations for the Fourier harmonic 1/2 amplitude distortion for three (3) optimal array designs arising from three (3) mission strategies. The data have been ordered such that the differences in each of the eighteen (18) matched pairs of CFD observations can be tested as a paired t-test. In a paired t-test, the mean of the sample difference and the standard deviation of the sample difference is calculated and the following t-statistic determined:

$$t^* = \frac{\left| \dfrac{1}{N} \sum_{j=1}^{N} \Delta_j \right|}{\sqrt{\displaystyle\sum_{j=1}^{n} \frac{(\Delta_j - \bar{\Delta})^2}{(N-1)}}} \quad (14)$$

where $\Delta_j = (Y_1 - Y_2)_j$ is the difference of each of the N-pairs of the response variable in the two data sets.

In the paired t-test, if the expression

$$t^* < t(0.975, \nu_p) \quad (15)$$

is valid, the response values from the first data set are not statistically different from the response values from the second data set at the 95% confidence level. Likewise, the response values from the first data set are statistically different from the response values from the second data set at the 95% confidence level if the expression

$$t^* > t(0.975, \nu_p) \quad (16)$$

Comparing the set of thee (3) Fourier micro-vane harmonic 1/2 amplitude profiles represented by Figure (19a) and the set of thee (3) Fourier micro-jet harmonic 1/2 amplitude profiles represented by Figure (19b), the mean of the sample difference MEAN = 0.0021 and the standard deviation of the sample difference STDEV = 0.0043. This gives a t-statistic $t^* = 0.4923$, which when compared to a t value $t(0.975, 17) = 2.110$, indicates there were no statistical significant differences between the two (2) sets of three (3) optimal cases at the 95% confidence level. Even though there are differences between the micro-vane and micro-jet the factor variables that define the optimal array designs, these factor differences did not translate into statistically significant differences in the Fourier harmonic 1/2 amplitudes of distortion. Therefore, no conclusions can be drawn as to the relative merits of optimal micro-vane arrays as compared to optimal micro-jet arrays in managing the Fourier harmonic 1/2 amplitudes of engine face distortion. There are no statistically significant differences.

Statistical Comparison of CFD Analysis and DOE Predictions

A direct statistical comparison can be made between the optimal responses predicted by the DOE models (Y_{DOE}) and the actual CFD predicted performance values (Y_{CFD}) through the t-statistic:

$$t^* = \frac{\left|(Y_{CFD}) - (Y_{DOE})\right|}{\dfrac{(Y_A) - (Y_{DOE})}{t(0.975, N-p)}} \quad (17)$$

where Y_A is the upper 95% confidence interval for the individual predicted response Y_{DOE} from the regression model, and t(0.975,N-p) is the 95% confidence t-value for N-p degrees of freedom. Equation (17) was used for the evaluation of the PFAVE regression model.

When there exists a functional relationship between the mean values and standard deviation of the data, the data do not satisfy the requirement that the variation is normally distributed. This often happens when there is a decade or more variation in the response variables range over the design (DOE) space. Under this condition, a transformation is often used to stabilize the variation over the response variable range. Because this was the case with DC60 and the first five Fourier harmonic 1/2-amplitudes, the natural logarithm of these responses were used in the DOE analysis and the t-statistic defined by

$$t^* = \frac{\left|\ln(Y_{CFD}) - \ln(Y_{DOE})\right|}{\dfrac{\ln(Y_A) - \ln(Y_{DOE})}{t(0.975, N-p)}} \quad (18)$$

was used in this evaluation of the (DC60) and the five Fourier harmonic 1/2-amplitude (F1/2, F2/2, F3/2, F4/2, F5/2) regression models.

For a statistically significant difference to exist between the DOE model predicted response (Y_{DOE}) and the CFD validation response prediction (Y_{CFD}), the expression:

$$t* > t(0.975, N - p) \qquad (19)$$

must hold. Likewise, if the expression

$$t* < t(0.975, N - p) \qquad (20)$$

is valid, the Y_{CFD} is not statistically different from Y_{DOE}. Therefore, for no significant statistical difference to exist between the DOE model predicted response Y_{DOE} and the CFD analysis response Y_{CFD}, the CFD response prediction must fall within the 95% confidence interval of the DOE model prediction for that response. For each "Optimal Robust" array design, the statistical comparisons were made between the corresponding responses for the cases in each set listed in Tables (10), and (11).

Table (12) presents the results of a statistical comparison between the CFD analysis and DOE predictions for the Maximum Performance, Maximum Engine Stability, and Maximum HCF Life Expectancy missions for the eight (8) response parameters. The eight response parameters include the inlet total pressure (PFAVE), the engine face distortion (DC60), the first five Fourier harmonic 1/2 amplitudes of distortion (F1/2, F2/2, F3/2, F4/2, F5/2), and the mean of the first five Fourier harmonic 1/2 amplitudes of distortion (FM/2). The results indicate that the DOE predictions were not significantly different from the CFD analysis results (i.e. the CFD analysis predictions fell within the 95% confidence interval of the DOE performance predictions). It also indicates that the optimal arrays determined by the DOE models were a statistically valid optima when compared to the actual CFD array analyses. The accuracy of the response surfaces determined from the DOE prediction was therefore sufficient for determining optimal array designs.

Impact of Jet Mass Flow (Wjet/Waip) on Optimal Array Performance

The significant terms in the DOE regression model for inlet total pressure recovery (PFAVE) are shown in Table (8), while the significant terms in the DOE regression model for the engine face distortion (DC60) are shown in Table (9). There were two important two-factor interaction identified for inlet total pressure recovery model and one important two-factor interaction identified for the DC60 distortion regression model. See Tables (8) and (9). For inlet total pressure recovery, the (Ap*Wjet/Waip) and (As*Wjet/Waip) interaction were significant, while the (As*Wjet/Waip) two-factor interaction was important for the engine face distortion regression model. There were many significant two-factor interaction associated with the Fourier harmonic 1/2 amplitudes of distortion, but these are not covered in this report. The significance of the factor interactions lies in the fact the optimal pitch angle (Ap) and optimal skew angle (As) will depend on the total amount of engine flow (Wjet/Waip) that is used to control the inlet flow field. This is illustrated in Figures (20) to (31), which presents the optimal inlet performance as a function of total jet mass flow (Wjet/Waip) used to manage the inlet flow for eight response parameters, i.e. the inlet total pressure recovery (PFAVE), engine face distortion (DC60), the first five Fourier harmonics 1/2 amplitudes of distortion (F1/2, F2/2, F3/2, F4/2, F5/2), and the mean of the first five Fourier harmonic 1/2 amplitudes of distortion (FM/2). Comparisons were made using the three mission strategies that are described in the section "Optimal Flow Control for Three Missions".

The three strategies are the Maximum Performance, Maximum Engine Stability, and Maximum HCF Life Expectancy missions.

Since the parameter number of micro-jet bands (Kbnd) statistically does not impact the optimal inlet performance, see Tables (8) and (9), the number of micro-jet bands was chosen to be one (1) for the optimal Maximum Performances designs, and five (5) for both the optimal Maximum Engine Stability and Maximum HCF Life Expectancy designs. See Figure (20). The choice for five bands for both the optimal Maximum Engine Stability and Maximum HCF Life Expectancy designs was intended in this report for illustration purposes only. If these inlets were to be tested, the one band for each design would have been chosen for economy reasons. Care must be taken in interpreting these findings, since this behavior is based on the condition that (Wjet/Waip) is constant. For example, if (Kjet) is chosen to be ten (10), it does not matter how many bands are chosen for the array design, provided the total jet mass flow use to manage the inlet flow (Wjet/Waip) is constant. Therefore, by increasing the number of micro-jet bands from one (1) to five (5), the individual micro-jet effector mass flow ratio (wjet/Waip) must correspondingly decrease in order to maintain a constant percent total jet mass flow ratio (Wjet/Waip). Figures (22) and (23) presents the effect of total jet mass flow ratio (Wjet/Waip) on the optimal values of pitch angle (Ap) and skew angle (As) for the three mission strategies. It is interesting to note the optimal pitch and skew angles depend on the mission strategy as well as the total jet mass flow ratio (Wjet/Waip) chosen to manage the inlet flow.

Figures (24) through (31) present the optimal inlet performance with respect to the eight response parameters of total pressure recovery (PFAVE), engine face distortion (DC60), the first five Fourier harmonics 1/2 amplitudes of distortion (F1/2, F2/2, F3/2, F4/2, F5/2), and the mean of the first five Fourier harmonic 1/2 amplitudes of distortion (FM/2) as a function of percent total jet mass flow ratio (Wjet/Waip). In comparing the effect of percent total jet mass flow (Wjet/Waip) on both total pressure recovery (PFAVE) and engine face distortion (DC60) characteristics, two dominate features stand out; namely (1) the very strong influence of (Wjet/Waip) on managing inlet performance, and (2) the three optimal micro-jet array designs provide essential the same inlet performance. See Figures (24) and (25). However, care must be taken in making judgements about the impact of (Wjet/Waip) on inlet performance. The penalties associated with bleeding high pressure engine flow to increase inlet total pressure recovery and decrease engine face distortion must be evaluated through a system study to determine the overall system benefit or penalty.

The similarity between optimal micro-vane array designs were also encountered and were studied by Anderson, Baust and Agrell[12]. Comparisons in that study indicated no statistically significant performance difference between the three optimal array micro-vane designs arising from the same three mission strategies used in this study.

Presented in Figures (26) through (31) are the effects of first five Fourier harmonics 1/2 amplitudes of distortion (F1/2, F2/2, F3/2, F4/2, F5/2), and the mean of the first five Fourier harmonic 1/2 amplitudes of distortion (FM/2) as a function of percent total jet mass flow ratio (Wjet/Waip). Again, the design parameter percent total jet mass flow (Wjet/Waip) has a dominant impact on managing the Fourier harmonic 1/2 amplitude of engine face distortion. It also appears that flow control does not necessarily mean the individual Fourier harmonic 1/2 amplitudes are improved over the baseline. This is indicated in Figures (28), (29), and (30), which show that flow control increased the third, fourth and fifth harmonic 1/2 amplitude of distortion relative to the baseline values in a portion of the total jet mass flow range. In general, the results presented in Figures (24) through (31) indicate that percent total jet mass flow ratio (Wjet/Waip) is the domi-

nant factor variable in managing the inlet flow field, and the optimal micro-jet array designs will always occur at the highest total jet mass flow value.

Grid Sensitivity Study for Inlet Performance

A grid sensitivity study was performed on three different micro-jet array configurations identified in Table (4). The three configuration represent individual jet mass flow ratios (wjet/Waip) of 0.10%, 0.01% and 0.001%. For each micro-jet configuration, two additional grid topologies were constructed represented by an inner grid (81x91x49) and an outer grid (81x361x49). The inner grid reduced the circumferential grid by 50% and the outer grid increased the circumferential grid by 100%.The conformation test cases for the computational grid study are presented in Table (13), while the performance results for the nine cases are presented in Table (14). The grid sensitivity study covered comparisons of the eight response variables, namely inlet total pressure recovery (PFAVE), engine face distortion (DC60), the first five Fourier harmonics 1/2 amplitudes of distortion (F1/2, F2/2, F3/2, F4/2, F5/2), and the mean of the first five Fourier harmonic 1/2 amplitudes of distortion (FM/2). A visual inspection of the numerical performance results for the eight response variables presented in Table (14) indicate remarkable similarity.

Figure (32) presents the engine face total pressure recovery contours for the nine conformation test cases defined in Table (13). Again, a visual inspection of the engine face contours indicate very small variations as a result of the three different computational grids. Presented in Figures (33) to (35) are the near wall streamlines for the three individual jet mass flow ratios (wjet/Waip) cases of 0.10%, 0.01% and 0.001% using the original grid from this study, i.e. configurations nvg401, nvg404, and nvg408. Each figure shows the both near wall inlet streamlines and the near wall streamlines in the micro-jet effector region.

A direct statistical comparison can be made between the responses predicted by the DOE models (Y_{DOE}) and the actual CFD predicted performance values from the ith grid $Y(i)_{CFD}$ through the expression:

$$t^* = \frac{\left|(Y(i)_{CFD}) - (Y_{DOE})\right|}{\dfrac{\ln(Y_A) - \ln(Y_{DOE})}{t(0.975, N - p)}} \qquad (21)$$

where Y_A is the upper 95% confidence interval for the individual predicted response Y_{DOE} from the regression model, and t(0.975,N-p) is the 95% confidence t-value for N-p degrees of freedom. Equation (21) was used for the evaluation of the PFAVE regression model.

As mentioned in a previous section, if there exists a functional relationship between the mean values and standard deviation of the data, the data do not satisfy the requirement that the variation is normally distributed. This often happens when there is a decade or more variation in the response variables range over the design (DOE) space. Under this condition, a transformation is often used to stabilize the variation over the response variable range. Because this was the case with DC60 and the first five Fourier harmonic 1/2-amplitudes, the natural logarithm of these responses were used in the DOE analysis and the t-statistic is consequently defined by

$$t^* = \frac{\left| \ln(Y(i)_{CFD}) - \ln(Y_{DOE}) \right|}{\dfrac{\ln(Y_A) - \ln(Y_{DOE})}{t(0.975, N - p)}} \qquad (22)$$

Equation (22) was used in this evaluation of the (DC60) and the five Fourier harmonic 1/2-amplitude (F1/2, F2/2, F3/2, F4/2, F5/2) regression models.

For a statistically significant difference to exist between the DOE model predicted response (Y_{DOE}) and the CFD validation response prediction (Y_{CFD}), the expression:

$$t^* > t(0.975, N - p) \qquad (23)$$

must hold. Likewise, if the expression

$$t^* < t(0.975, N - p) \qquad (24)$$

is valid, the $Y(i)_{CFD}$ is not statistically different from Y_{DOE}. Therefore, for no significant statistical difference to exist between the DOE model predicted response Y_{DOE} and the CFD analysis response from the ith grid $Y(i)_{CFD}$, the CFD response prediction must fall within the 95% confidence interval of the DOE model prediction for that response.

Table (15) and (16) presents the results of a statistical comparison between the CFD analysis from the inner grid (81x91x49) and outer grid (81x361x49) and DOE predictions generated by the response surface from the center grid (81x181x49). The eight response parameters include in this statistical comparison are the inlet total pressure (PFAVE), the engine face distortion (DC60), the first five Fourier harmonic 1/2 amplitudes of distortion (F1/2, F2/2, F3/2, F4/2, F5/2), and the mean of the first five Fourier harmonic 1/2 amplitudes of distortion (FM/2). The CFD analysis predictions from both inner and outer grid topologies fell within the 95% confidence interval of the DOE performance predictions generated from the response surfaces of the center grid. However, for those three cases in which a statistical difference were indicated, the actual differences between the CFD analysis and DOE prediction were small relative to experimental error. Therefore, the accuracy of the response surfaces generated by the computational grid in the present study was more than adequate for use in determining optimal array designs. In fact, these results also indicate that the inner grid (81x91x49) could have been used in the DOE study to generate the response surfaces, saving substantial amounts of computational run time, without sacrificing statistical accuracy.

CONCLUSIONS

The fundamental importance of *Response Surface Methods* over traditional design approaches lies in the optimal sequenced pattern of Design-of-Experiments (DOE), the statistical model building, and the systematic procedures for the optimization of design configurations. *Response Surface Methods* allows the numbe*r* of CFD case run to be optimized, depending on the program objectives, for a substantial reduction in the number of CFD experiments to be run. This strategy is superior to the traditional approach of changing one variable at a time because this does

not permit the estimation of the two-factor interactions. The 27 runs of the present DOE is also more economical than a full factorial approach where the number of experiments would be 3^5 or 243 separate cases. RSM also provides an economical, reliable and systematic approach to variable screening as well as the general exploration of the region that contains the estimated optimal conditions. As a result, the pragmatic use of RSM places a high priority on obtaining a better understanding of the process system as well as estimating the optimum conditions. In the design of micro-scale secondary flow arrays for compact inlets, it is just as important to understand and quantify the behavior of the factor (design) parameters in the neighborhood of the optimal conditions as knowing the optimal conditions. Hence, an RSM approach is particularly beneficial for the design of micro-jet arrays since there are a great many factor (design) variables available to the aerodynamicist, and often there exists multiple design objectives. Also multiple mission optimal arrays were determined with *Response Surface Methods* without repeating the optimization procedure.

The use micro-jet actuation in the revised M2129 S-duct was dominated by the factor (design) variable total jet mass flow (Wjet/Waip) used to manage the inlet flow. Between total jet mass flow ratios (Wjet/Waip) of 0.10% and 1.0% the optimal value would always be at the highest value, or 1.0%, unless the penalties associated with bleeding high pressure engine flow are taken into account. The total jet mass flow (Wjet/Waip) also effected the optimal pitch (Ap) and skew angle (As) through the factor interactions (Ap*Wjet/Waip) and (As*Wjet/Waip). In general, the higher the total jet mass flow (Wjet/Waip) the lower the optimal pitch angle (Ap) and skew angle (As). The performance of the micro-jet arrays was also effected by the number of micro-jets per band (Kjet), but not by the number of micro-jet bands (Kbnd). This characteristics held only under the condition of fixed total jet mass flow ratio (Wjet/Waip). The optimal number of micro-jets per band (Kjet) always favored the fewest number of jets at constant (Wjet/Waip). Acceptable inlet distortion (DC60) characteristics were also achieved in the revised M2129 inlet duct at total jet mass flow ratios (Wjet/Waip) as low as 0.50%. The use micro-jet actuation in the revised M2129 S-duct was also very effective in managing the Fourier harmonic 1/2 amplitude content of engine face distortion.

To illustrate the potential of *Response Surface Methods,* three different mission strategies were considered for the subject inlet, namely (1) Maximum Performance, (2) Maximum Engine Stability, and (3) Maximum HCF Life Expectancy. The Maximum Performance mission minimized the inlet total pressure losses, the Maximum Engine Stability mission minimized the engine face distortion (DC60), while the Maximum HCF Life Expectancy mission minimized the mean of the first five Fourier harmonic amplitudes, i.e. "collectively" reduced all the harmonic 1/2-amplitudes of engine face distortion. By visually comparing the CFD validation performance of the three optimal arrays designs, i.e. Maximum Performance, Maximum Engine Stability, and the Maximum HCF Life Expectancy, it is obvious that they are remarkably similar. Also, a visual comparison between the performance of the three optimal arrays designs determined by the DOE prediction and the CFD validation analysis shows remarkable similarity. A comparison between optimal arrays determined by the DOE prediction and CFD analysis indicates statistically differences occurred about 8% of the time, which is remarkably good. All the cases in which a statistical difference were indicated involved the evaluation of the Fourier harmonic 1/2-amplitudes of distortion. In these particular cases, the differences between the CFD analysis and DOE prediction were to too small to be of practical significance, i.e. they could not be experimentally measured. This indicates that the DOE prediction results were not statistically different from the CFD analysis results (i.e. the CFD analysis predictions fell within the 95% confidence interval of the

DOE performance predictions). It also indicated that the optimal arrays determined by the DOE models were a statistically valid optima when compared to the actual CFD array analyses. The accuracy of the response surfaces determined from the DOE analysis was therefore more than adequate for use in determining an array optimum.

A comparison between the set of three (3) optimal micro-jet arrays and the set of three (3) optimal micro-vane arrays indicates a substantial increase in total pressure recovery as a result of the using micro-jet arrays. However, care must be taken in making judgements about micro-jets vs. micro-vane as the penalty for bleeding high pressure engine flow has not been included in this study. Excellent engine face distortion characteristics were also achieved with the micro-effector units, i.e both micro-jet and micro-vanes. Essentially no performance differences were evident between micro-vanes and micro-jet arrays with regards to engine face distortion. A paired t-test comparison between the set of thee (3) optimal Fourier micro-vane harmonic 1/2 amplitude profiles and the set of thee (3) Fourier micro-jet harmonic 1/2 amplitude profiles indicated no statistical significant differences between the two (2) sets of three (3) optimal cases at the 95% confidence level. Even though there are differences between the micro-vane and micro-jet the factor variables that define the optimal array designs, these factor differences did not translate into statistically significant differences in the Fourier harmonic 1/2 amplitudes of distortion.

REFERENCES

[1] Anderson, B. H., Miller, D. N., Yagle, P. J, and Truax, P. P., "A Study of MEMS Flow Control for the Management of Engine Face Distortion in Compact Inlet Systems", FEDSM99-69220, 3rd ASME/JSME Joint Fluids Engineering Conference, San Francisco, CA,   July 18-23, 1999.

[2] Hamstra, J. W., Miller, D. N., Truax, P. P., Anderson, B. H., and Wendt, B. J., "Active Inlet Flow Control Technology Demonstration," ICAS-2000-6.11.2, 22nd International Congress of the Aeronautical Sciences, Harrogate, UK, August 27th-September 1st, 2000.

[3] Box, G. E. P., and Jones, S., "*Empirical Model Building and Response Surfaces*," John Wiley, New York, 1987.

[4] Box, G. E. P., Hunter, W. G., and Hunter, J. S., "*Statistics for Experimenters*," John Wiley, New York, 1978.

[5] Anderson, B. H., Miller, D. N., Addington, G. A., and Agrell, J., "The Role of Robust Optimization in Managing Flow in Compact Air Vehicle Inlets," Propose NASA TM, 2003.

[6] AGARD FTP Working Group 13, "Air Intakes for High Speed Vehicles", AR-270, September 1991.

[7] Willmer, A. C., Brown, T. W. and Goldsmith, E. L., "Effects of Intake Geometry on Circular Pitot Intake Performance at Zero and Low Forward Speeds", Aerodynamics of Power Plant Installation, AGARD CP301, Paper 5, Toulouse, France, May 1981, pp 51-56.

[8] Bray, T. P., "A Parametric Study of Vane and Air-jet Votrex Generators", Ph'd Thesis, College of Aeronautics, Cranfield University, Oct. 1998.

[9] Gibb, J and Jackson, M., "Vortex Flow control for the management of intake duct flow distortion - results of the M2129 Phase 4 test in the DRA Bedford 13' by 9' wind tunnel", DRA/Report, DRA/AS/HWA/CR942121/1, August, 1994.

[10] Gibb, J., Jackson, M., "The use of air-jet vortex generators for the control of aircrat intake distortion", DRA Report, DRA/AS/HWA/CR95187/1, August, 1995.

[11] Bray, T. P., Wier, B., and Gigg, J., "Experimental evaluation of inlet distortion management at flight Reynolds number (M2129 Phase 9)", DERA/MSS/MSFC2/CR990134, June, 1999.

[12] Anderson, B. H., Baust, H. D., and Agrell, J., "Management of Total Pressure Recovery, Distortion, and High Cycle Fatique in Compact Air Vehicle Inlets," NASA/TM-2002-212000, Dec. 2002.

[13] Bender, E. E, Anderson, B. H., and Yagle, P. J., "Vortex Generator Modeling for Navier Stokes Code", FEDSM99-69219, 3rd ASME/JSME Joint Fluids Engineering Conference, San Francisco, CA, July 18-23, 1999.

[14] Ludwig, G. R., "Aeroelastic Considerations in the Measurement of Inlet Distortion", 3rd National Turbine Engine High Cycle Fatigue Conference, 1998.

[15] Anderson, B. H. and Keller, D. J., "Considerations in the Measurements of Engine Face Distortion for High Cycle Fatigue in Compact Inlet Diffusers", NASA/M-2001-211476, March 2001.

[16] Goldsmith, E. L., and Seddon, J. (eds), "*Practical Intake Aerodynamics*," Blackwell Scientific Publications, Oxford, 1993.
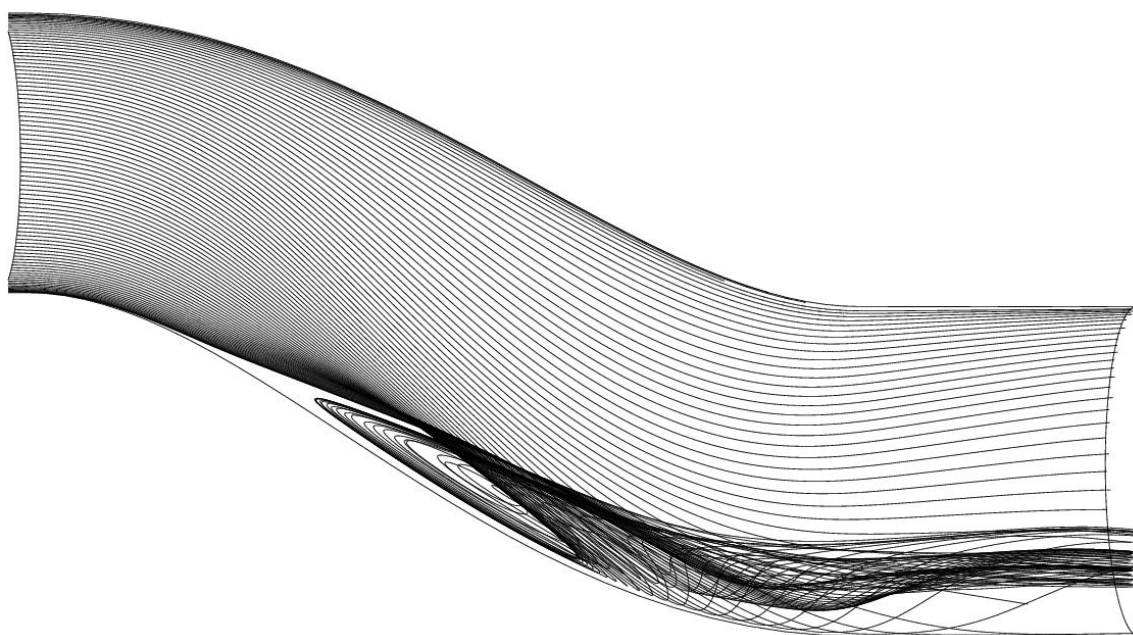
Figure (1): Near wall streamlines in baseline inlet S-duct, Mt = 0.70, α = 0.0 (degs).
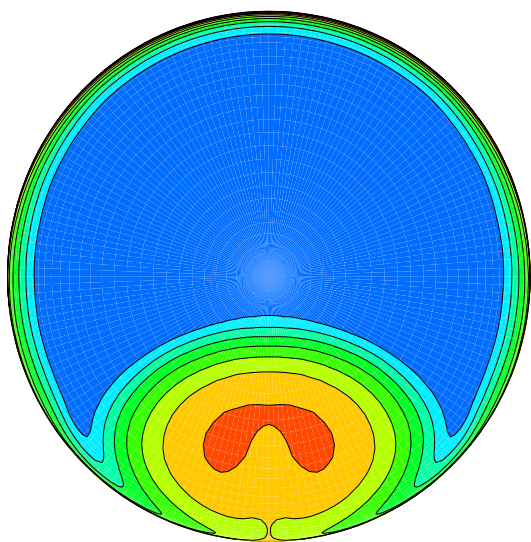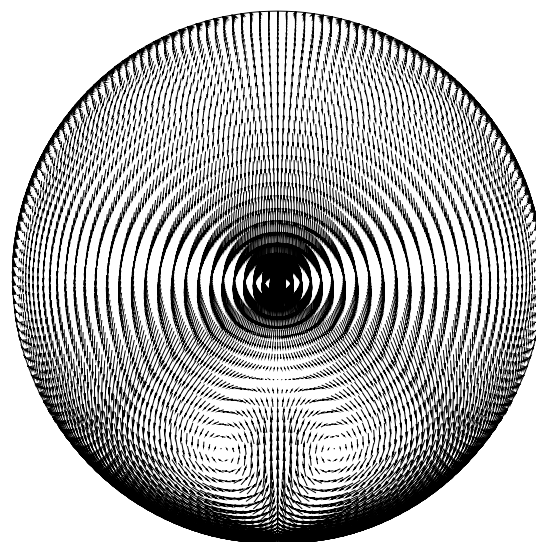
(a) Total Pressure Recovery Contours   **(b) Secondary Velocity Vectors**

Figure (2): Engine face flow field in baseline inlet S-duct, Mt = 0.70, α = 0.0 (degs).

X_{aip} = 15.0

x=2.985
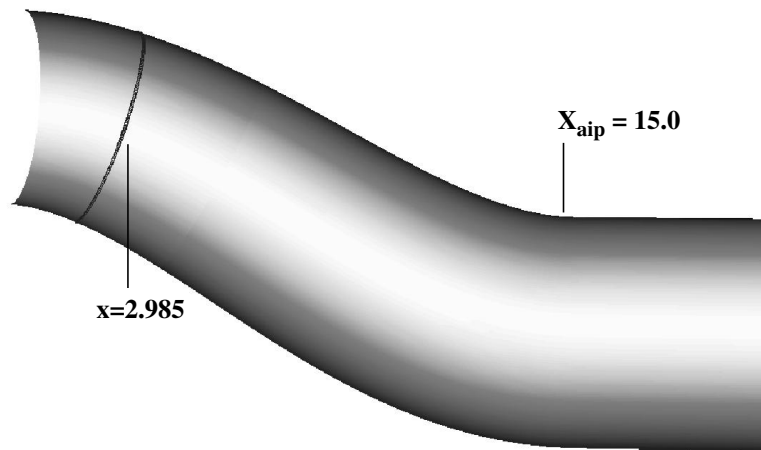
(a) Single band micro-jet array concept, Kbnd = 1

X_{aip} = 15.0

x=4.605
x=2.895
x=1.365
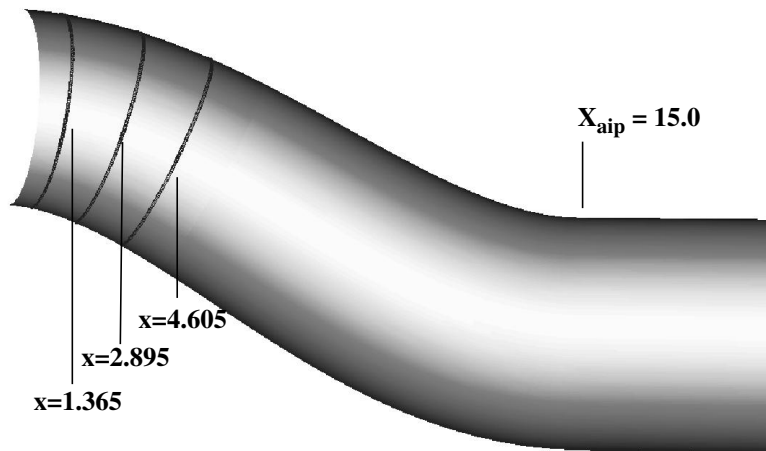
(b) Three band micro-jet array concept, Kbnd = 3

X_{aip} = 15.0

x=4.605
x=3.773
x=2.985
x=2.198
x=1.365
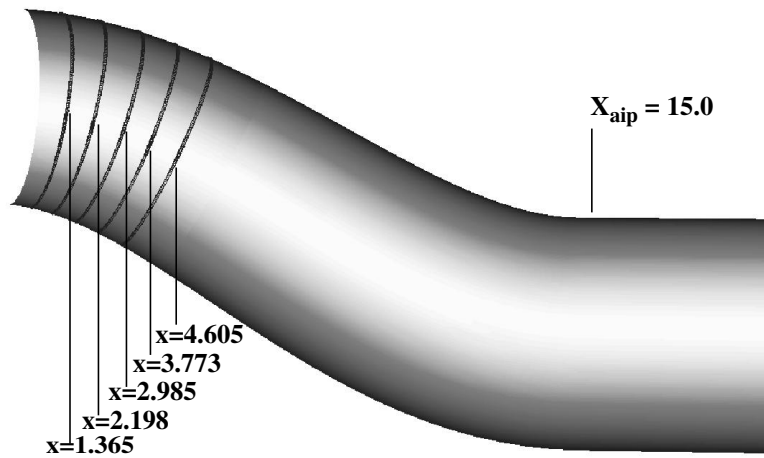
(c) Five band micro-jet array concept, Kbnd = 5
Figure (3): Location of micro-jet band arrays (inches) within inlet.

.

Factor	Range
Number of Micro-Jet Bands, Kbnd	1 to 5
Number of Micro-Jets per Band, Kjet	10.0 to 20.0
Micro-Jet Pitch Angle (degs.), Ap	15.0 to 45.0
Micro-Jet Skew Angle (degs.), As	30.0 to 60.0
%Total Jet Mass Flow Ratio, Wjet/Waip	0.10% to 1.00%

Table (1): Factor variables which establish the DOE design matrix.

Variable	Value
Inlet Throat Mach Number, Mi	0.70
Inlet Total Pressure (lbs/ft^2), Pt	10506.0
Inlet Total Temperature (^{o}R), Tt	517.0
Inlet Reynolds Number per ft., Rey	2.02×10^7
Micro-Jet Total Pressure (Bar), Pjet	3.0

Table (2): Variables held constant.

Response	Nomenclature
Engine Face Total Pressure Recovery	PFAVE
Engine Face Distortion	DC60
1st Fourier Harmonic 1/2-Amplitude	F1/2
2nd Fourier Harmonic 1/2-Amplitude	F2/2
3rd Fourier Harmonic 1/2-Amplitude	F3/2
4th Fourier Harmonic 1/2-Amplitude	F4/2
5th Fourier Harmonic 1/2-Amplitude	F5/2

Table (3): DOE response variable.
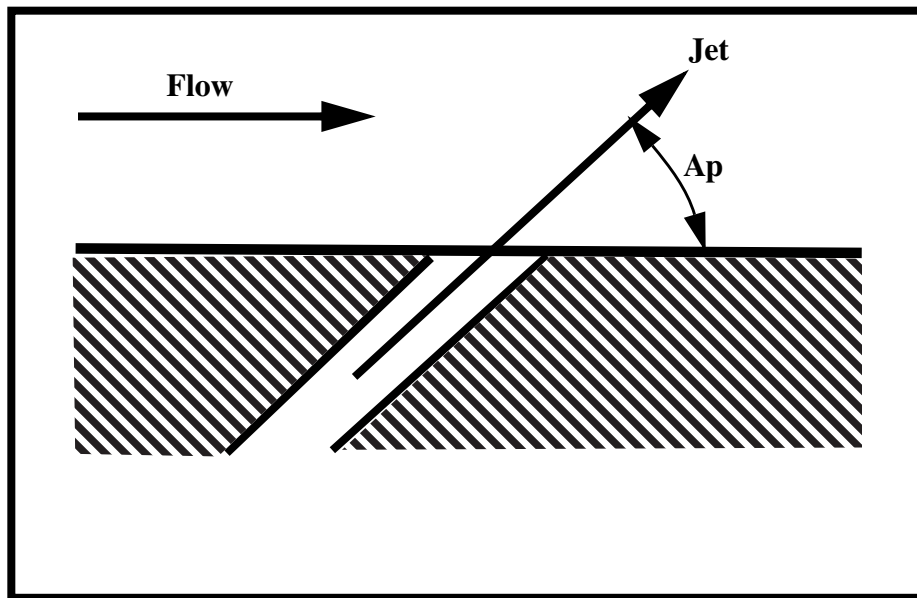
Figure (4): Schematic diagram showing micro-jet geometry pitch angle (Ap) definition, side view.
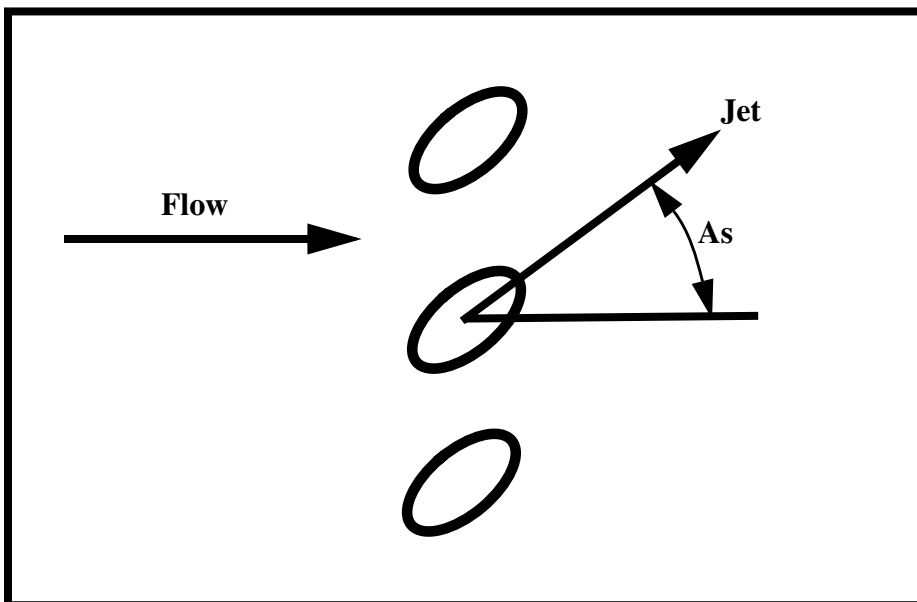
Figure (5): Schematic diagram showing micro-jet geometry skew angle (As) definition, top view.

Config.	Kbnd	Kjet	Ap	As	% Wjet/Waip
nvg401	1.0	10.0	15.0	30.0	1.00
nvg402	5.0	10.0	15.0	30.0	0.10
nvg403	1.0	20.0	15.0	30.0	0.10
nvg404	5.0	20.0	15.0	30.0	1.00
nvg405	1.0	10.0	45.0	30.0	0.10
nvg406	5.0	10.0	45.0	30.0	1.00
nvg407	1.0	20.0	45.0	30.0	1.00
nvg408	5.0	20.0	45.0	30.0	0.10
nvg409	1.0	10.0	15.0	60.0	0.10
nvg410	5.0	10.0	15.0	60.0	1.00
nvg411	1.0	20.0	15.0	60.0	1.00
nvg412	5.0	20.0	15.0	60.0	0.10
nvg413	1.0	10.0	45.0	60.0	1.00
nvg414	5.0	10.0	45.0	60.0	0.10
nvg415	1.0	20.0	45.0	60.0	0.10
nvg416	5.0	20.0	45.0	60.0	1.00
nvg417	1.0	15.0	30.0	45.0	0.55
nvg418	5.0	15.0	30.0	45.0	0.55
nvg419	3.0	10.0	30.0	45.0	0.55
nvg420	3.0	20.0	30.0	45.0	0.55
nvg421	3.0	15.0	15.0	45.0	0.55
nvg422	3.0	15.0	45.0	45.0	0.55
nvg423	3.0	15.0	30.0	30.0	0.55
nvg424	3.0	15.0	30.0	60.0	0.55
nvg425	3.0	15.0	30.0	45.0	0.10
nvg426	3.0	15.0	30.0	45.0	1.00
nvg427	3.0	15.0	30.0	45.0	0.55

Table (4): Central Composite Face-Centered (CCF) Design-of-Experiments matrix.
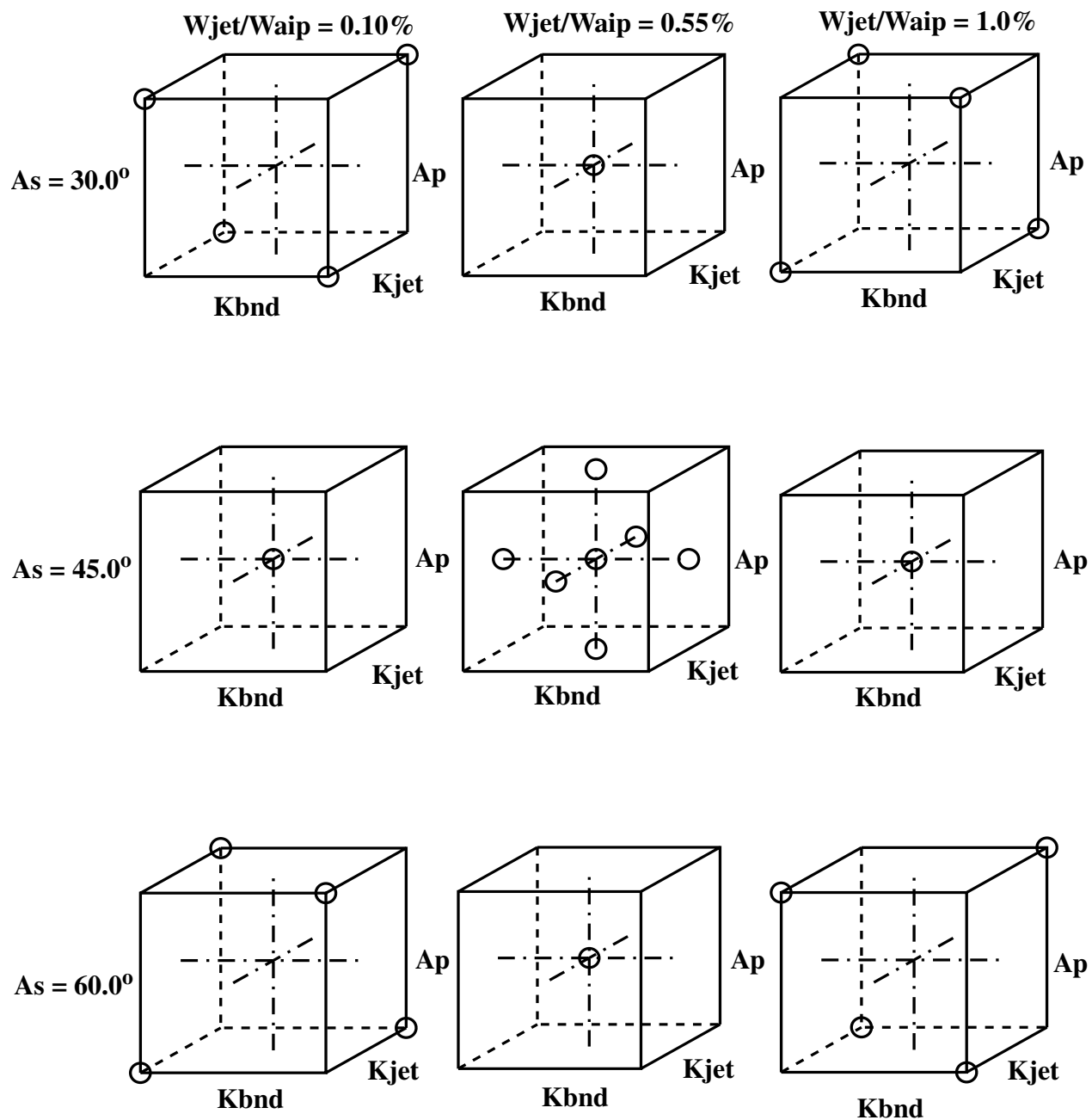
Figure (6): Graphical representation of the Central Composite Face-Centered (CCF) Design-of-Experiments matrix.

Ring Number	Radial Weighting Coefficient
1	0.05651
2	0.14248
3	0.21077
4	0.26918
5	0.32106

Table (5): Radial weighting coefficients applied to the total pressure rake measurements.
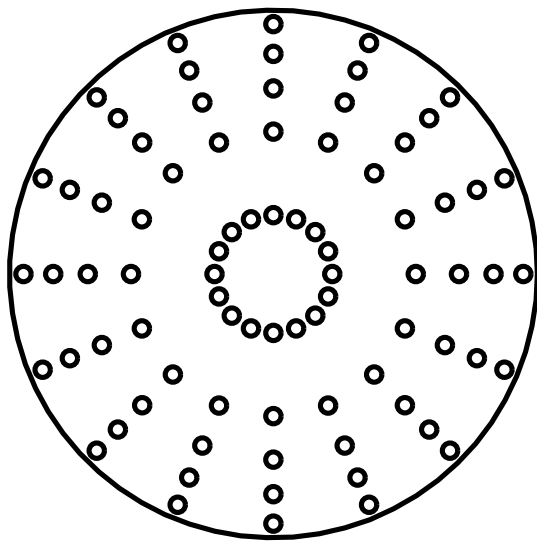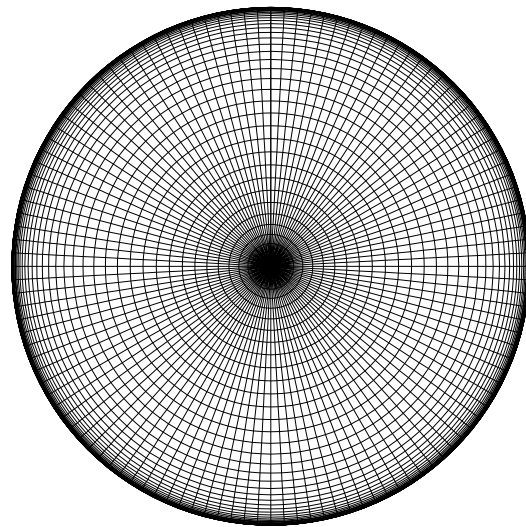
(a) 80-probe rake   **(b) Computational grid**

Figure (7): Total pressure and distortion measurement arrays.

Response	Nomenclature	S^2_{max}/S^2_{min}	$F(0.975,9,9)$
1st Harmonic 1/2-Amplitude	F1/2	1017.8	4.03
2nd Harmonic 1/2-Amplitude	F2/2	2980.6	4.03
3rd Harmonic 1/2-Amplitude	F3/2	378.76	4.03
4th Harmonic 1/2-Amplitude	F4/2	114.30	4.03
5th Harmonic 1/2-Amplitude	F5/2	2097.5	4.03

Table (6): Fourier Harmonic 1/2-amplitude F-test compliance

Config.	PFAVE	DC(60)	F1/2	F2/2	F3/2	F4/2	F5/2
nvg401	0.98712	0.04698	0.00232	0.00191	0.00878	0.00110	0.00494
nvg402	0.97273	0.35188	0.03092	0.02675	0.01600	0.00103	0.00336
nvg403	0.97178	0.36309	0.03224	0.02767	0.01606	0.00134	0.00382
nvg404	0.98646	0.04889	0.00400	0.00985	0.00877	0.00096	0.00089
nvg405	0.97235	0.37961	0.02960	0.02674	0.01764	0.00202	0.00174
nvg406	0.98333	0.04667	0.00324	0.00253	0.00710	0.00514	0.00384
nvg407	0.98182	0.06730	0.00598	0.00411	0.01142	0.00698	0.00485
nvg408	0.97093	0.38311	0.03260	0.02824	0.01676	0.00449	0.00341
nvg409	0.97509	0.32402	0.02560	0.02375	0.01596	0.00610	0.00209
nvg410	0.98352	0.05235	0.01004	0.01147	0.00676	0.00329	0.00067
nvg411	0.98334	0.07230	0.01340	0.01468	0.00313	0.00719	0.00298
nvg412	0.97282	0.31482	0.02930	0.02497	0.01340	0.00751	0.00311
nvg413	0.97907	0.08320	0.00331	0.00964	0.01560	0.00751	0.00311
nvg414	0.97320	0.33092	0.02682	0.02477	0.01642	0.00582	0.00204
nvg415	0.97206	0.34769	0.03025	0.02655	0.01583	0.00434	0.00348
nvg416	0.97670	0.08753	0.00516	0.01252	0.01693	0.00360	0.00320
nvg417	0.98145	0.08406	0.00941	0.00088	0.00917	0.00833	0.00721
nvg418	0.98144	0.08012	0.00746	0.00385	0.01274	0.00828	0.00411
nvg419	0.98258	0.06482	0.00108	0.00241	0.00939	0.00794	0.00512
nvg420	0.98021	0.09670	0.01029	0.00090	0.01240	0.01055	0.00734
nvg421	0.98201	0.07619	0.00515	0.00583	0.01366	0.00795	0.00404
nvg422	0.97670	0.13879	0.01882	0.01036	0.00473	0.01170	0.01325
nvg423	0.98106	0.10491	0.01310	0.00625	0.00579	0.01205	0.01075
nvg424	0.97907	0.09099	0.00857	0.00510	0.01480	0.00918	0.00528
nvg425	0.97254	0.33670	0.03041	0.02621	0.01512	0.00333	0.00417
nvg426	0.98475	0.05325	0.00762	0.01183	0.00717	0.00330	0.00138
nvg427	0.98059	0.10108	0.01066	0.00105	0.01261	0.01099	0.00740

Table (7: Engine face performance results for the Central Composite Face-Centered (CCF) Design-of-Experiments matrix.
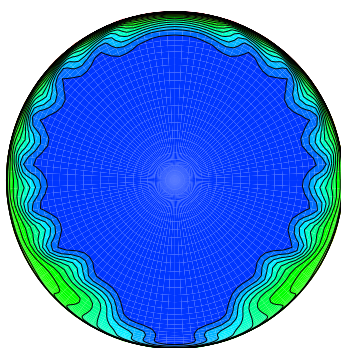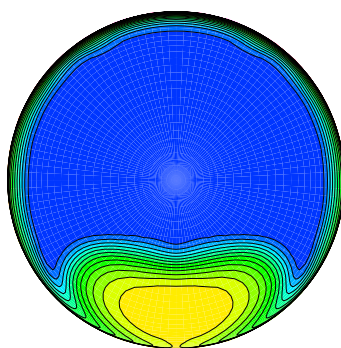
Config. nvg401   **Config. nvg402**   **Config. nvg403**
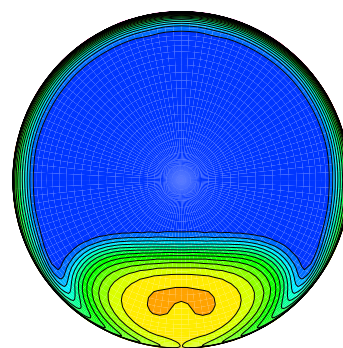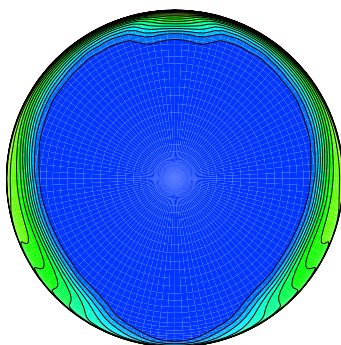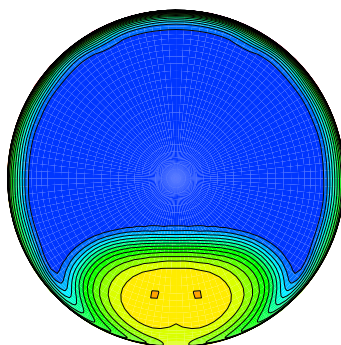
Config. nvg404   **Config. nvg405**   **Config. nvg406**
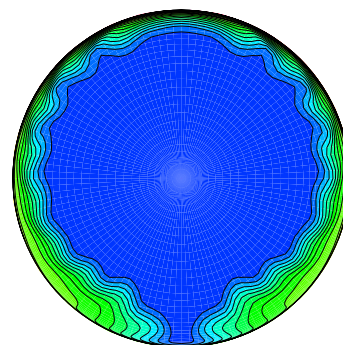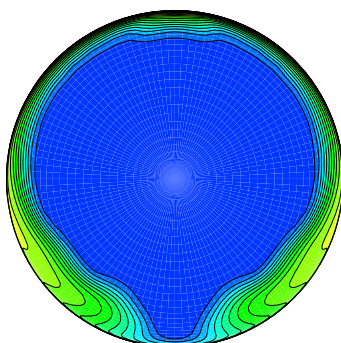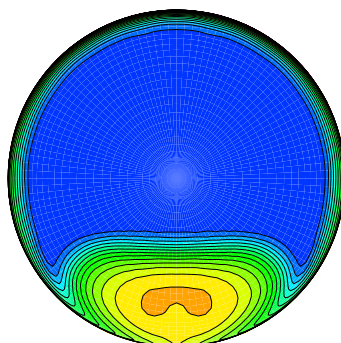
Config. nvg407   **Config. nvg408**   **Config. nvg409**
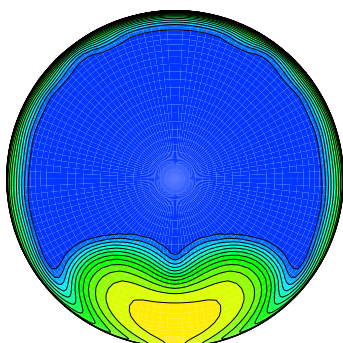
Figure (8): Engine face total pressure recovery contours for the Central Composite Face-Centered (CCF) Design-of-Experiments matrix.
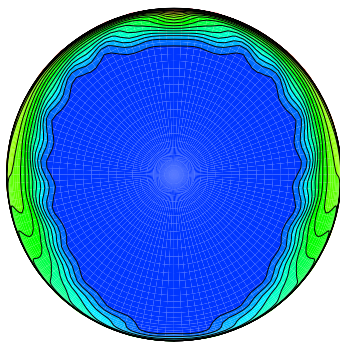
Config. nvg410
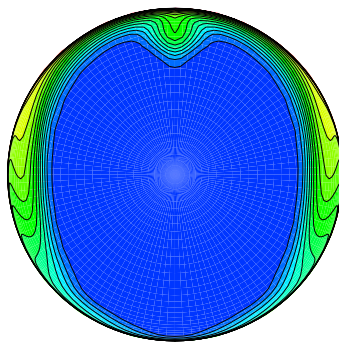
Config. nvg411
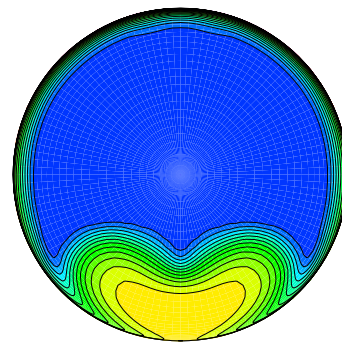
Config. nvg412
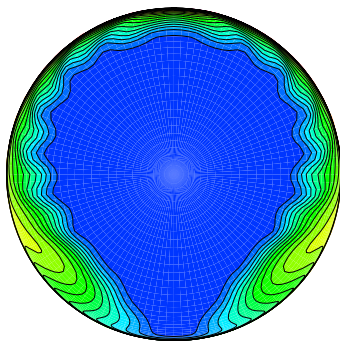
Config. nvg413
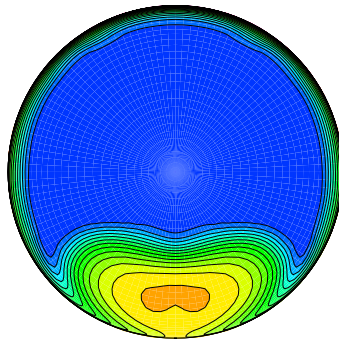
Config. nvg414
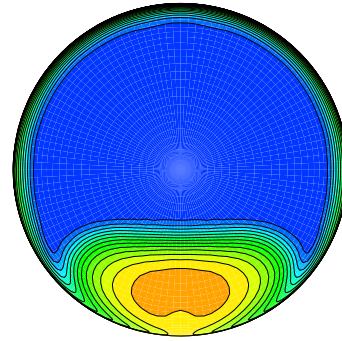
Config. nvg415
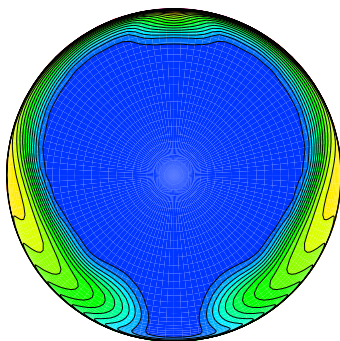
Config. nvg416
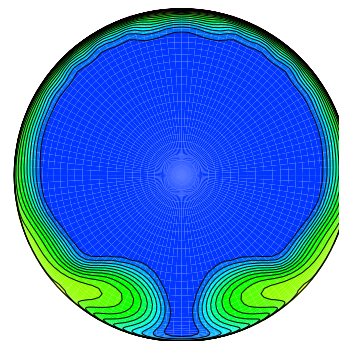
Config. nvg417
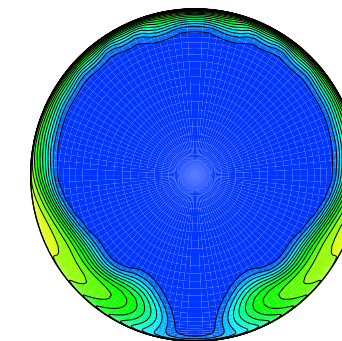
Config. nvg418

Figure (8): Engine face total pressure recovery contours for the Central Composite Face-Centered (CCF) Design-of-Experiments matrix, continued.
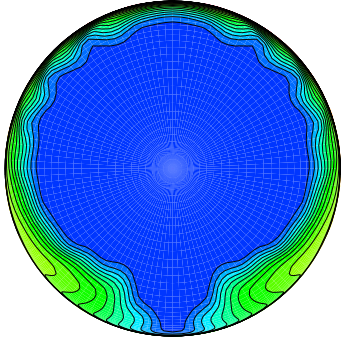
Config. nvg419
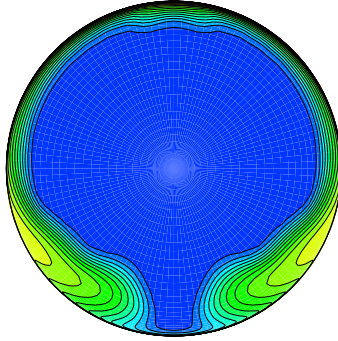
Config. nvg420
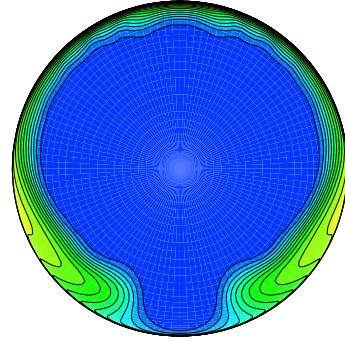
Config. nvg421
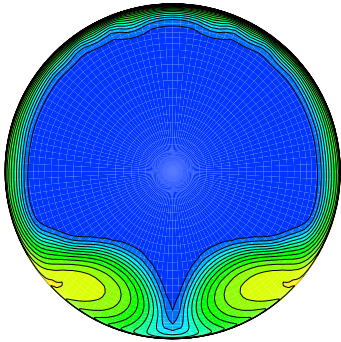
Config. nvg422
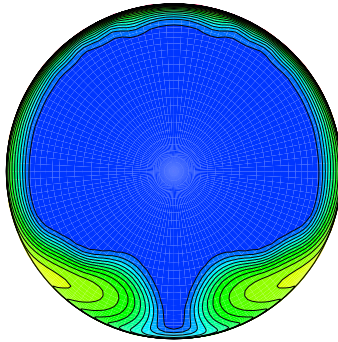
Config. nvg423
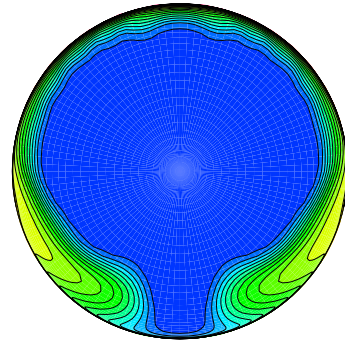
Config. nvg424
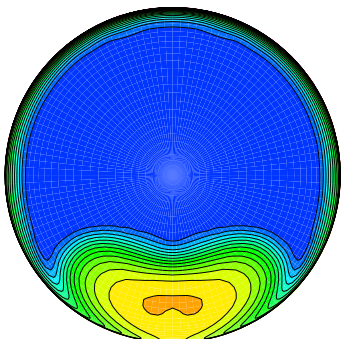
Config. nvg425
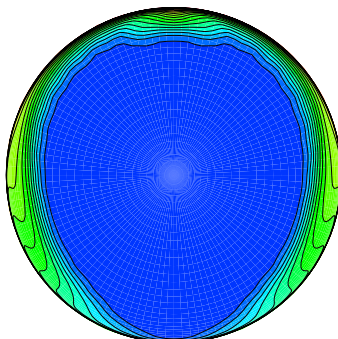
Config. nvg426
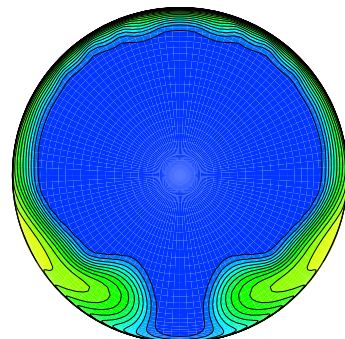
Config. nvg427

Figure (8): Engine face total pressure recovery contours for the Central Composite Face-Centered (CCF) Design-of-Experiments matrix, concluded.

Term	Transf. Coeff.	p	% Signif.
1	0.980971	0.0001	99.99
Kjet	-0.000668	0.0053	99.47
Ap	-0.001588	0.0001	99.99
As	-0.000707	0.0024	99.76
Wjet/Waip	0.005144	0.0001	99.99
Ap*(Wjet/Waip)	-0.000977	0.0002	99.98
As*(Wjet/Waip)	-0.001343	0.0001	99.99
$Kjet^2$	0.001186	0.0433	95.67
Ap^2	-0.001478	0.0123	98.77
As^2	-0.000813	0.1402	85.98
$(Wjet/Waip)^2$	-0.002233	0.0006	99.94

Table (8): Significance of regression terms in DOE model for inlet total pressure recovery, PFAVE.

Term	Transf. Coeff.	p	% Signif.
1	-2.422757	0.0001	99.99
Ap	0.100948	0.0100	99.90
Wjet/Waip	-0.875113	0.0001	99.99
As*(Wjet/Waip)	0.112491	0.0073	99.27
Ap^2	0.119623	0.1638	83.62
$(Wjet/Waip)^2$	0.383622	0.0001	99.99

Table (9): Significance of regression terms in DOE model for engine face distortion, DC60.
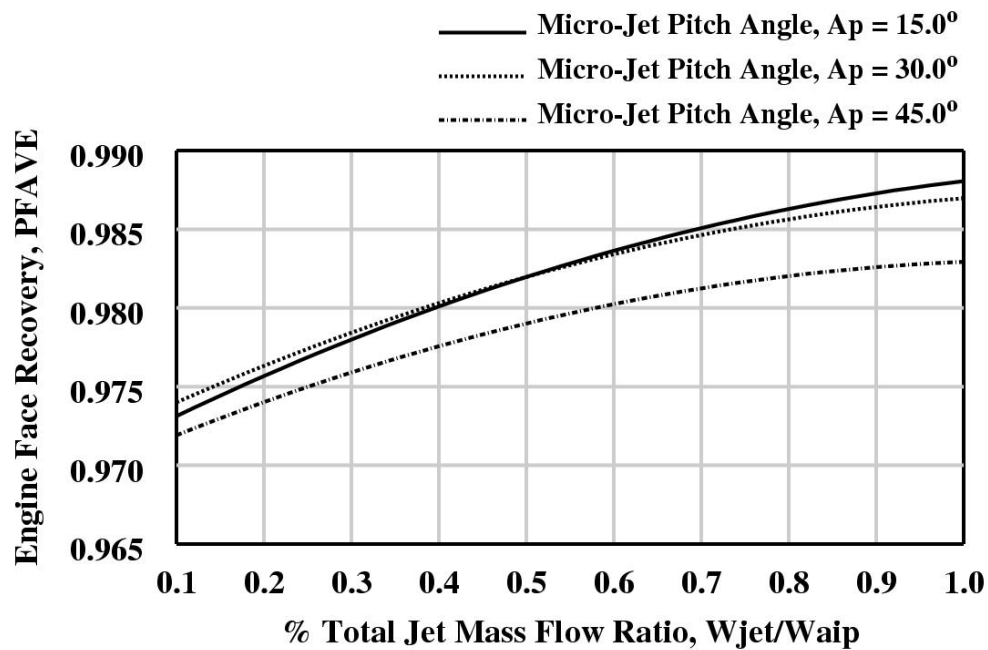
Figure (9): Effect of the (Ap*(Wjet/Waip) interaction on inlet total pressure recovery (PFAVE), Kbnd = 5, Kjet = 10, As = 30.0°.
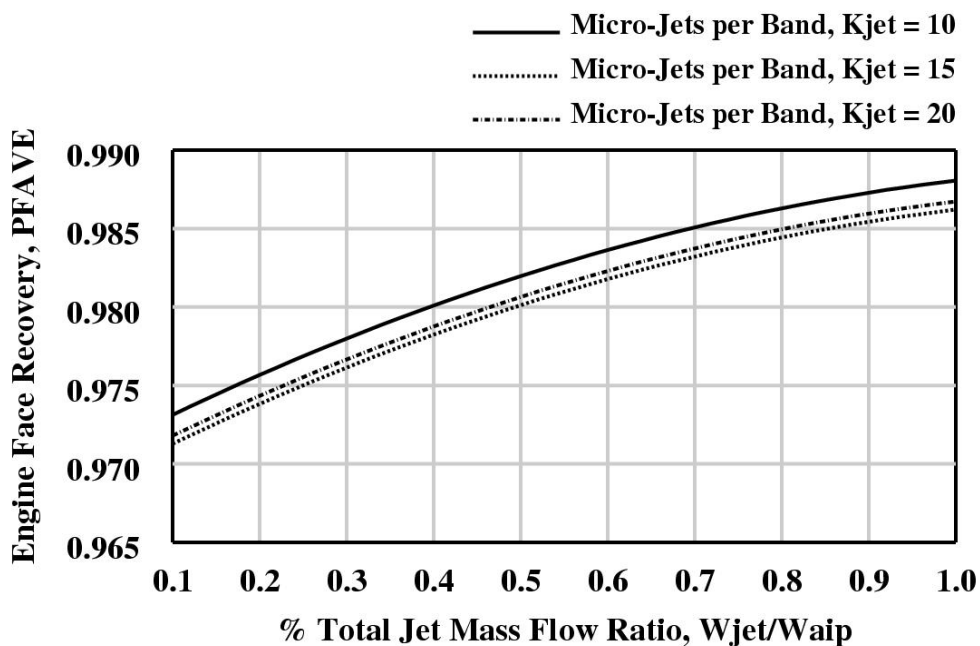
Figure (10): Effect of (Wjet/Waip) on inlet total pressure recovery (PFAVE), Kbnd = 5, Ap = 15.0°, As = 30.0°
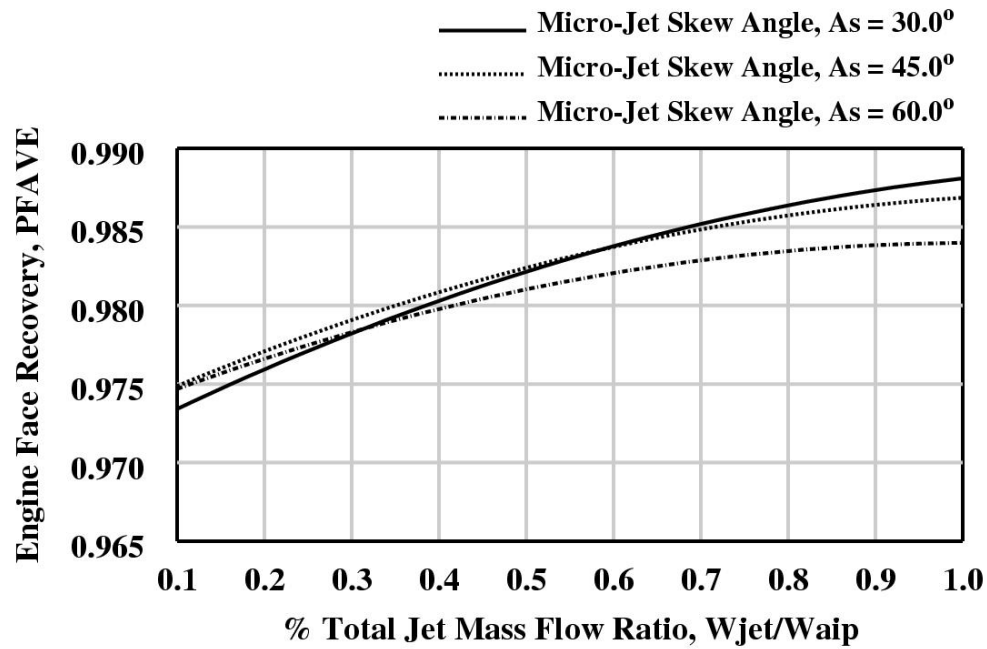
Figure (11): Effect of the (As*(Wjet/Waip) interaction on inlet total pressure recovery, (PFAVE), Kbnd = 5, Kjet = 10, Ap = 15.0°.
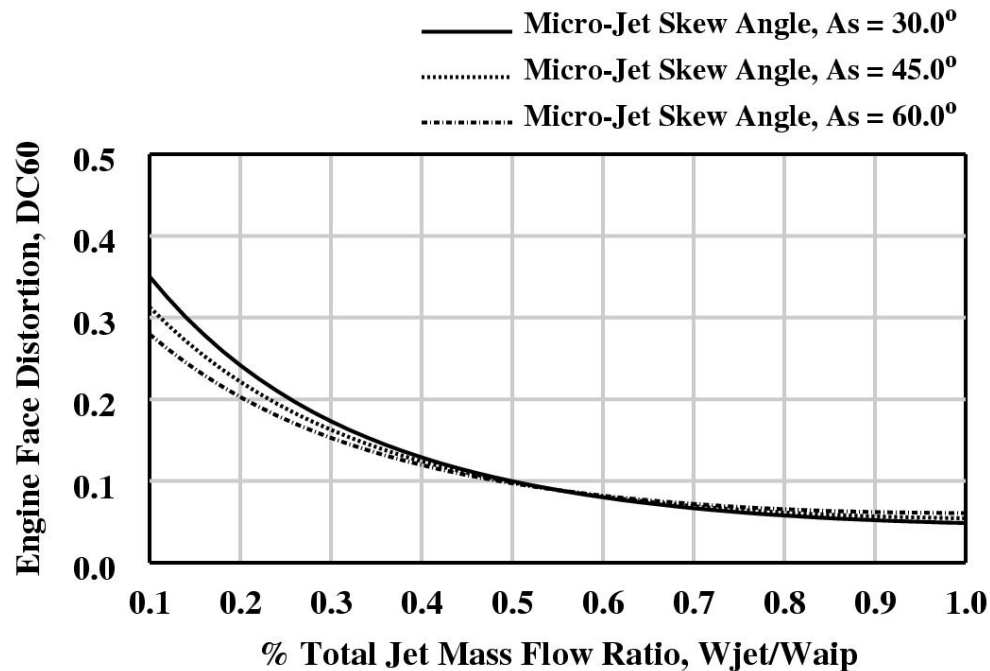
Figure (12): Effect of the (As*(Wjet/Waip) interaction on engine face distortion, (DC60), Kbnd = 5, Kjet = 10, Ap = 15.0°.

Factor/Response	Max. Perf.	Max. Stability	Max. HCF Life
Kbnd	1	5	5
Kjet	10	10	10
Ap (degs.)	17.0	23.7	15.5
As (degs.)	30.0	30.0	40.1
Wjet/Waip	1.0%	1.0%	1.0%
PFAVE	0.98809	0.98779	0.98742
DC60	0.04859	0.04745	0.05304
F1/2	0.00180	0.00193	0.00186
F2/2	0.00143	0.00177	0.00253
F3/2	0.00866	0.00860	0.00614
F4/2	0.00535	0.00293	0.00269
F5/2	0.00352	0.00165	0.00087

Table (10): Engine face performance DOE predictions for optimal micro-jet secondary flow control array designs.

Factor/Response	Max. Perf.	Max. Stability	Max. HCF Life
Kbnd	1	5	5
Kjet	10	10	10
Ap (degs.)	17.0	23.7	15.5
As (degs.)	30.0	30.0	40.1
Wjet/Waip	1.0%	1.0%	1.0%
PFAVE	0.98693	0.98703	0.98646
DC60	0.04134	0.03327	0.04704
F1/2	0.00130	0.00245	0.00406
F2/2	0.00341	0.00445	0.00664
F3/2	0.00884	0.00781	0.00789
F4/2	0.00430	0.00297	0.00189
F5/2	0.00351	0.00192	0.00090

Table (11): Engine face performance CFD solutions for optimal micro-jet secondary flow control array designs.
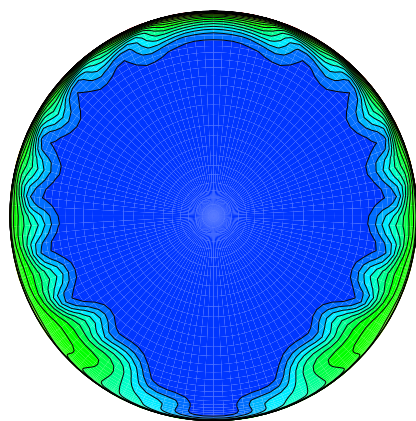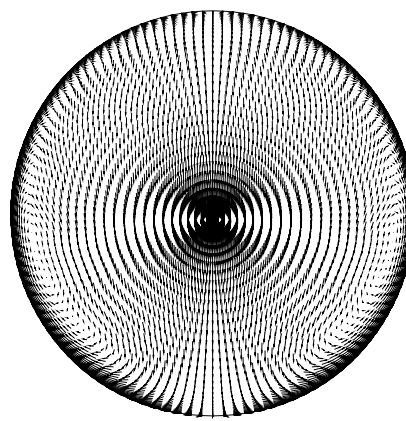
Total Pressure Recovery   **Secondary Flow**

(a) Optimal Maximum Performance array
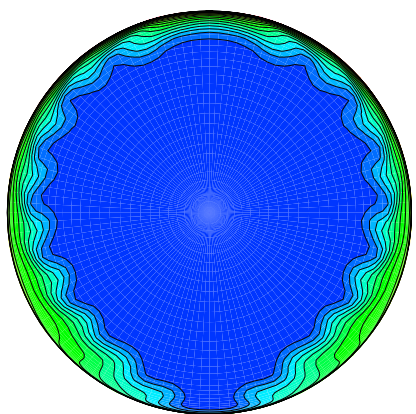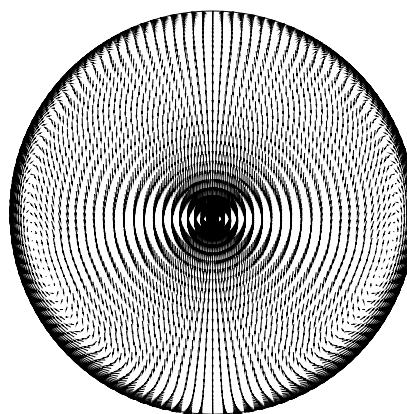
Total Pressure Recovery   **Secondary Flow**

(b) Optimal Maximum Engine Stability array
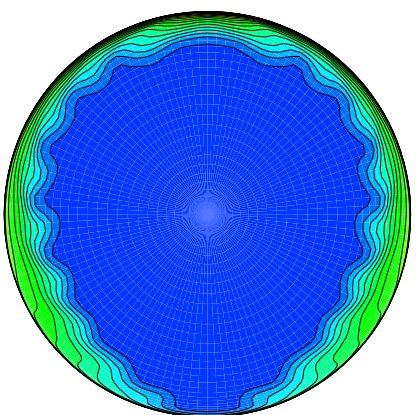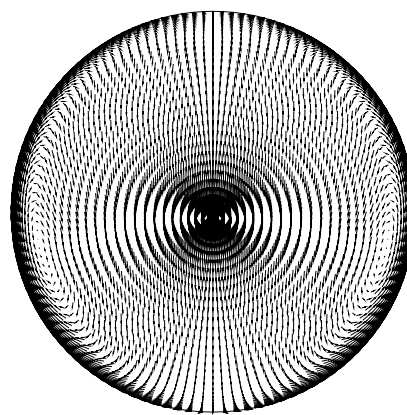
Total Pressure Recovery   **Secondary Flow**

(c) Optimal HCF Life Expectancy array

Figure (13): Engine face CFD solutions for optimal micro-jet secondary flow control array designs, Mt = 0.70, α = 0.0^o.
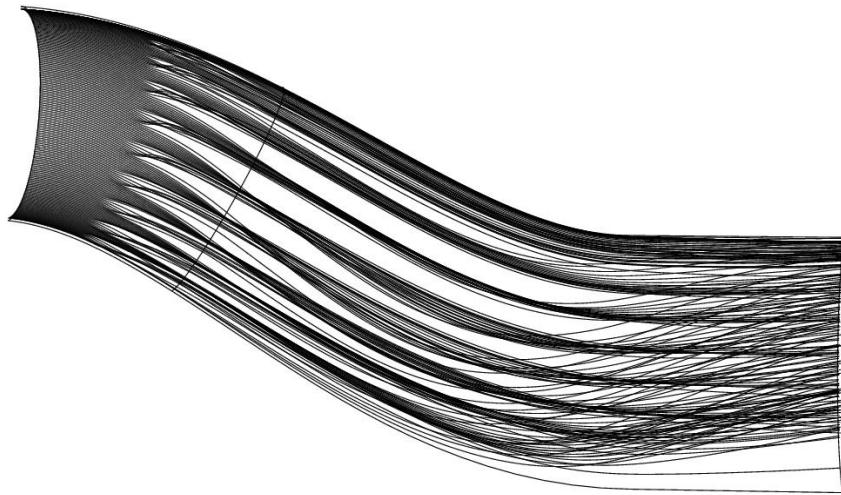
(a) Inlet near wall streamlines.
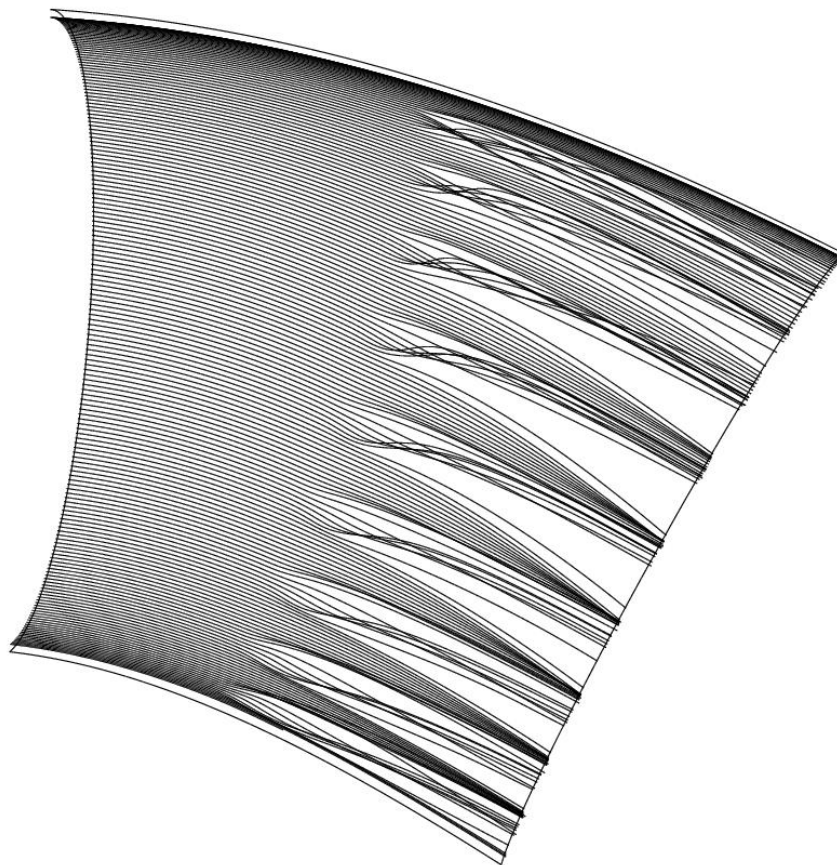
(b) Effector region near wall streamlines.

Figure (14): Near wall streamlines for Optimal Maximum Performance micro-jet array, Wjet/Waip = 1.0%, wjet/Waip = 0.10%.
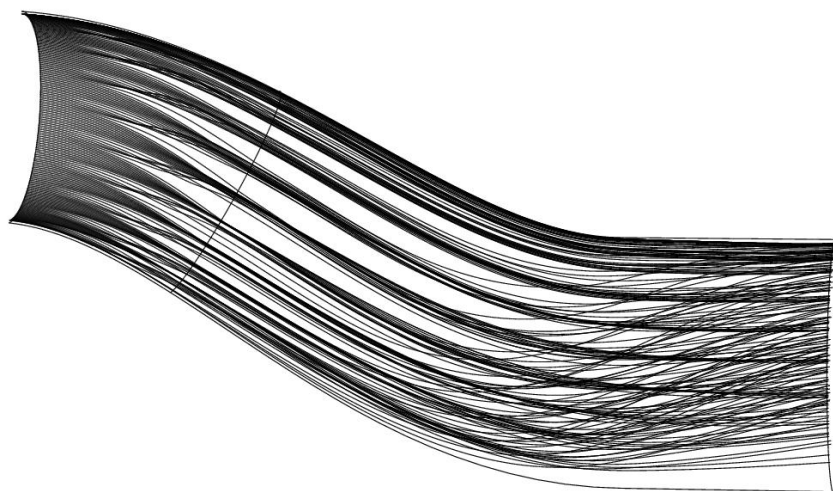
(a) Inlet near wall streamlines.
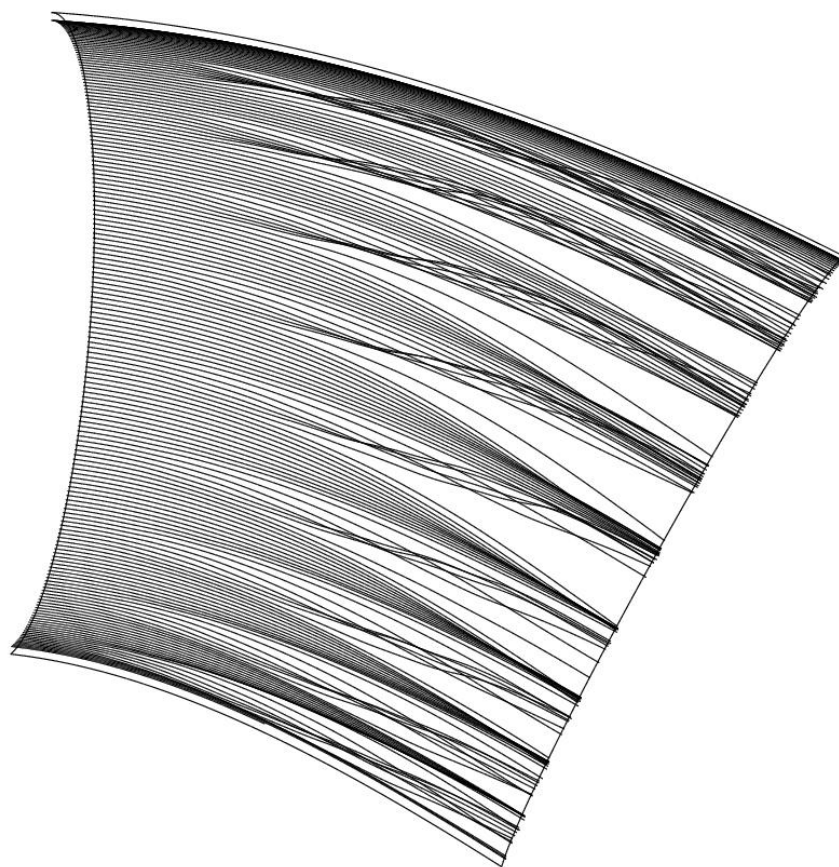
(b) Effector region near wall streamlines.

Figure (15): Near wall streamlines for Optimal Maximum Engine Stability micro-jet array, Wjet/Waip = 1.0%, wjet/Waip = 0.02%.
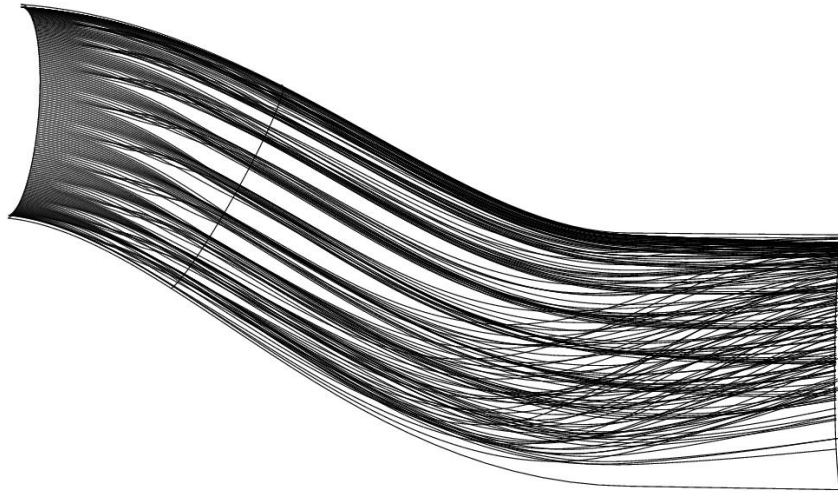
(a) Inlet near wall streamlines.
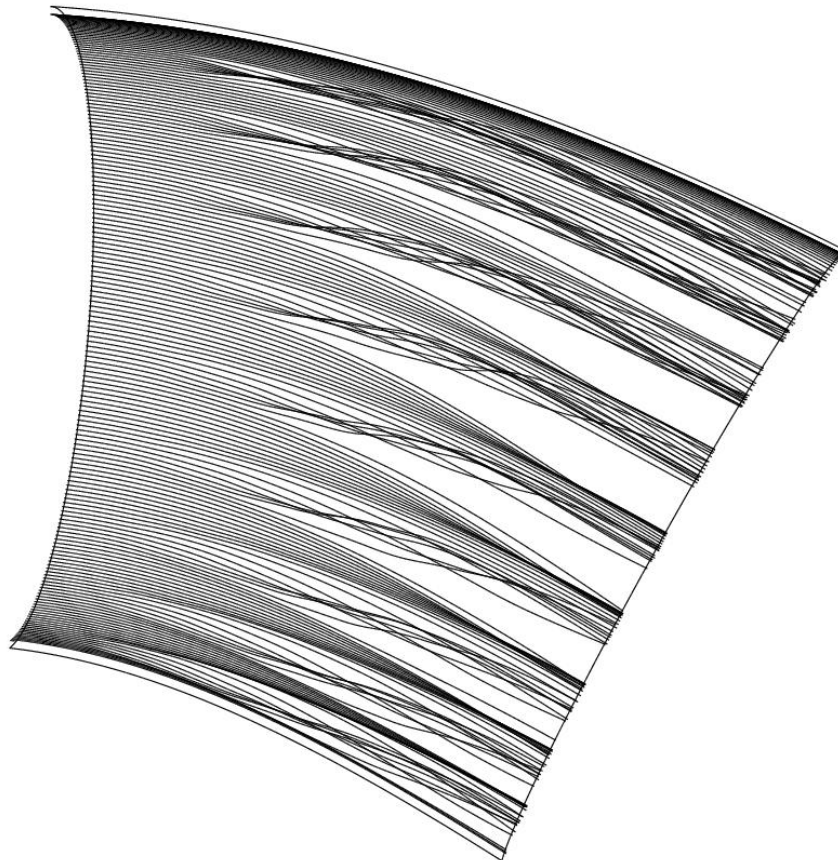
(b) Effector region near wall streamlines.

Figure (16): Near wall streamlines for Optimal Maximum HCF Life Expectancy micro-jet array, Wjet/Waip = 1.0%, wjet/Waip = 0.02%.
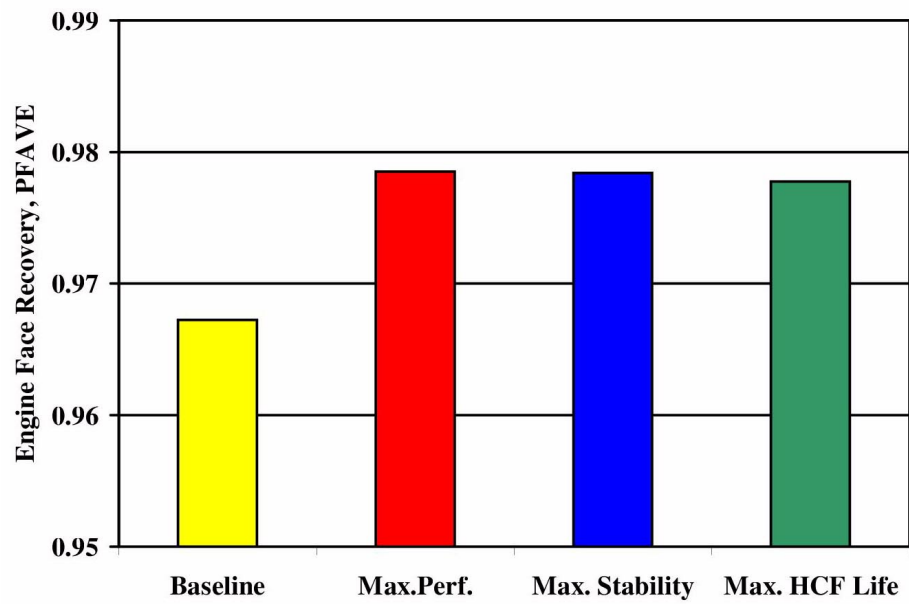
(a) Optimal micro-vane effector arrays.
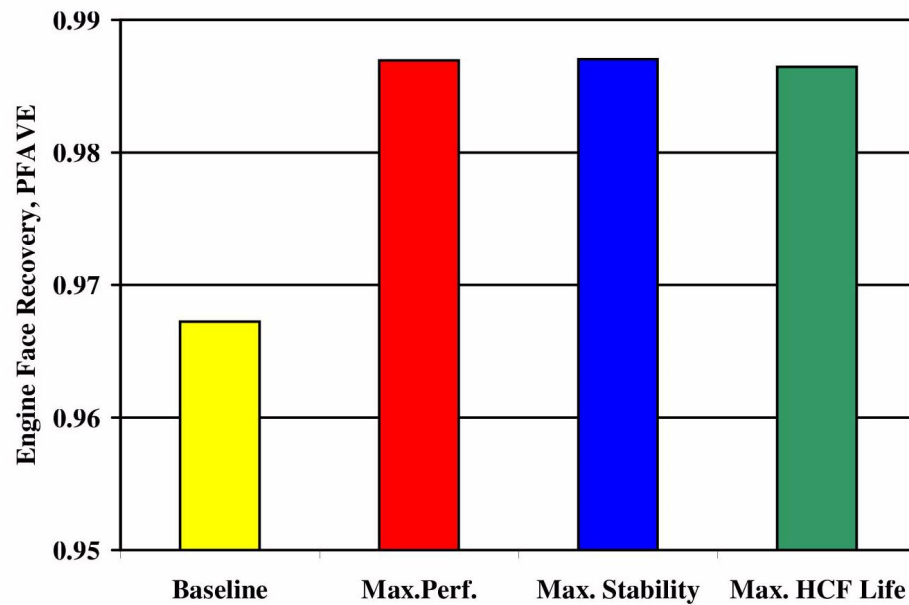
(b) Optimal micro-jet effector arrays.

Figure (17): Effect of optimal micro-effector array designs on the inlet total pressure recovery (PFAVE), Mt = 0.70, α = 0.0^o.
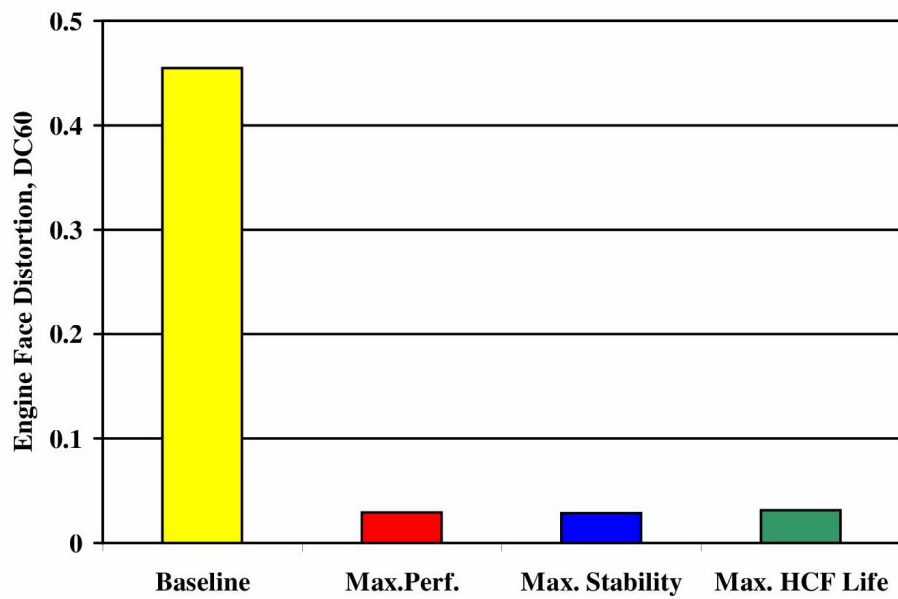
(a) Optimal micro-vane effector arrays.
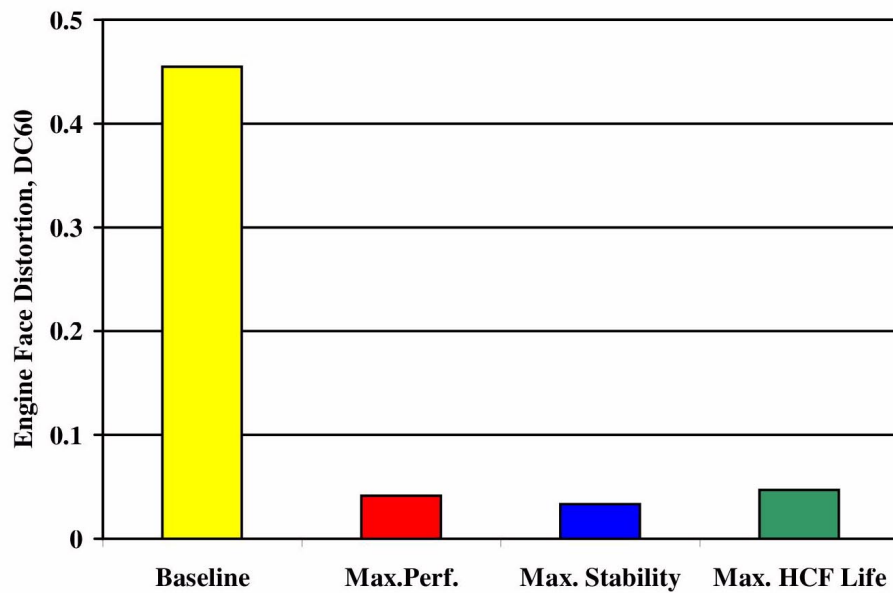
(b) Optimal micro-jet effector installations.

Figure (18): Effect of optimal micro-effector array designs on the engine face distortion (DC60), Mt = 0.7, $\alpha = 0.0^o$.
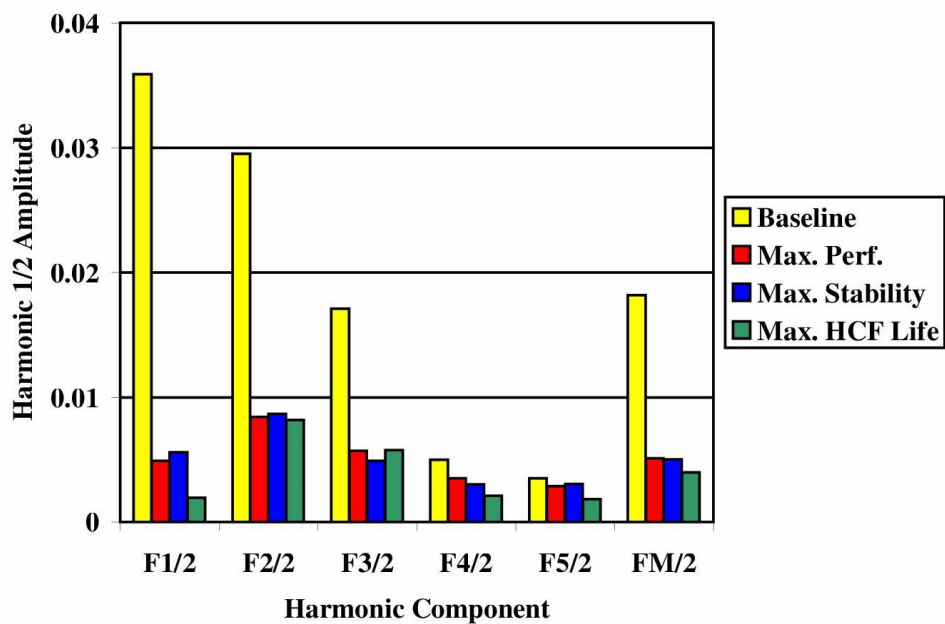
(a) Optimal micro-vane effector installations.
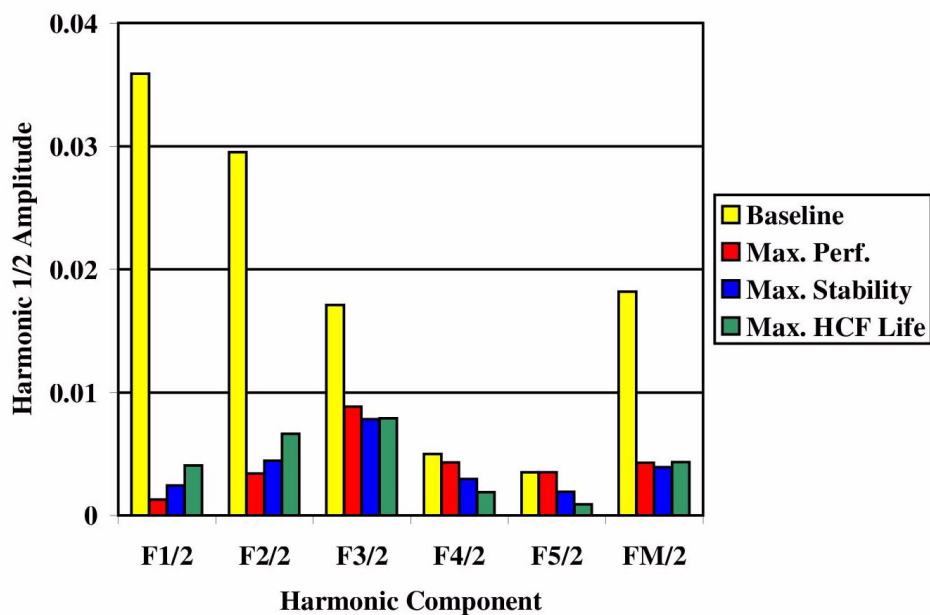
(b) Optimal micro-jet effector installations.

Figure (19): Effect of optimal micro-effector array designs on the Fourier harmonic 1/2 amplitudes of distortion (Fk/2), Mt = 0.70, $\alpha = 0.0^o$.

Response	Installation	CFD	DOE	t	t*	Comments
PFAVE	Max. Perf.	0.98693	0.98809	2.11991	1.18226	Not Diff.
DC60		0.04134	0.04859	2.02961	0.94299	Not Diff.
F1/2		0.00130	0.00180	1.96920	0.73785	Not Diff.
F2/2		0.00341	0.00143	1.96927	1.94319	Not Diff.
F3/2		0.00884	0.00866	1.96927	0.08918	Not Diff.
F4/2		0.00430	0.00535	1.96931	0.99063	Not Diff.
F5/2		0.00351	0.00352	1.96931	0.00827	Not Diff.
FM/2		0.00427	0.00415	1.96920	0.08363	Not Diff.
PFAVE	Max. Stability	0.98703	0.98779	2.11991	0.72248	Not Diff.
DC60		0.03327	0.04745	2.02961	1.98066	Not Diff.
F1/2		0.00245	0.00193	1.96920	0.56695	Not Diff.
F2/2		0.00445	0.00177	1.96927	1.83912	Not Diff.
F3/2		0.00781	0.00860	1.96927	0.40816	Not Diff.
F4/2		0.00297	0.00293	1.96931	0.05782	Not Diff.
F5/2		0.00192	0.00165	1.96931	0.45057	Not Diff.
FM/2		0.00392	0.00337	1.96920	0.39001	Not Diff.
PFAVE	Max. HCF Life	0.98646	0.98742	2.11991	0.90853	Not Diff.
DC60		0.04704	0.05304	2.02961	0.71573	Not Diff.
F1/2		0.00406	0.00186	1.96920	1.82918	Not Diff.
F2/2		0.00664	0.00253	1.96927	1.93048	Not Diff.
F3/2		0.00789	0.00614	1.96927	1.04259	Not Diff.
F4/2		0.00189	0.00269	1.96931	1.53558	Not Diff.
F5/2		0.00090	0.00087	1.96931	0.27766	Not Diff.
FM/2		0.00414	0.00282	1.96920	0.84521	Not Diff.

Table (12): Statistical comparison between CFD analysis and DOE prediction for the optimal micro-jet installation designs.
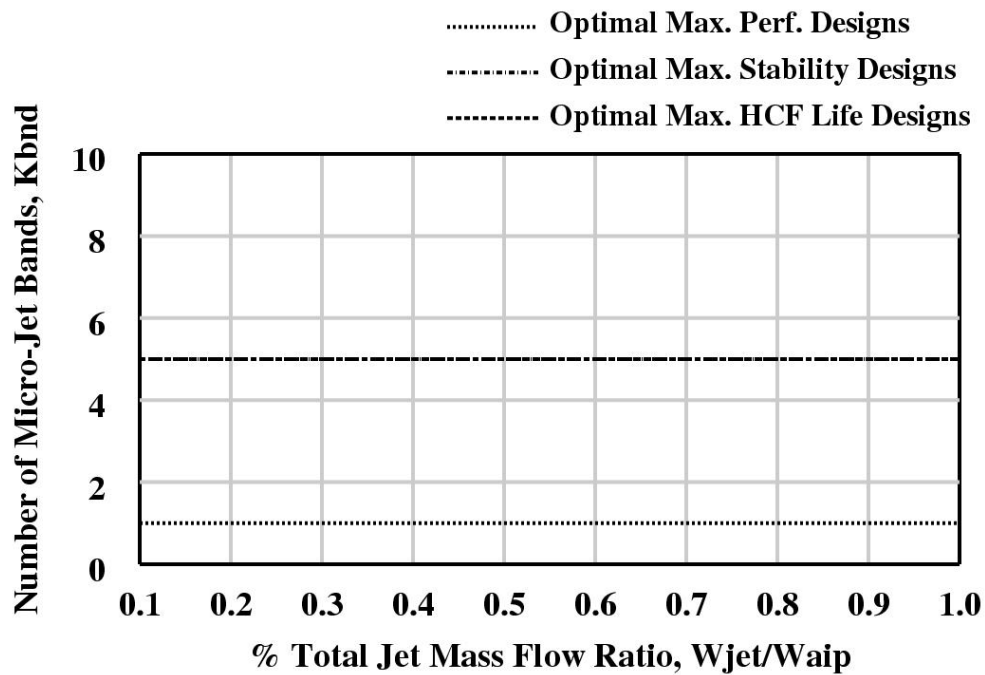
Figure (20): Effect of percent total jet mass flow ratio (Wjet/Waip on optimal number of micro-jet band settings.
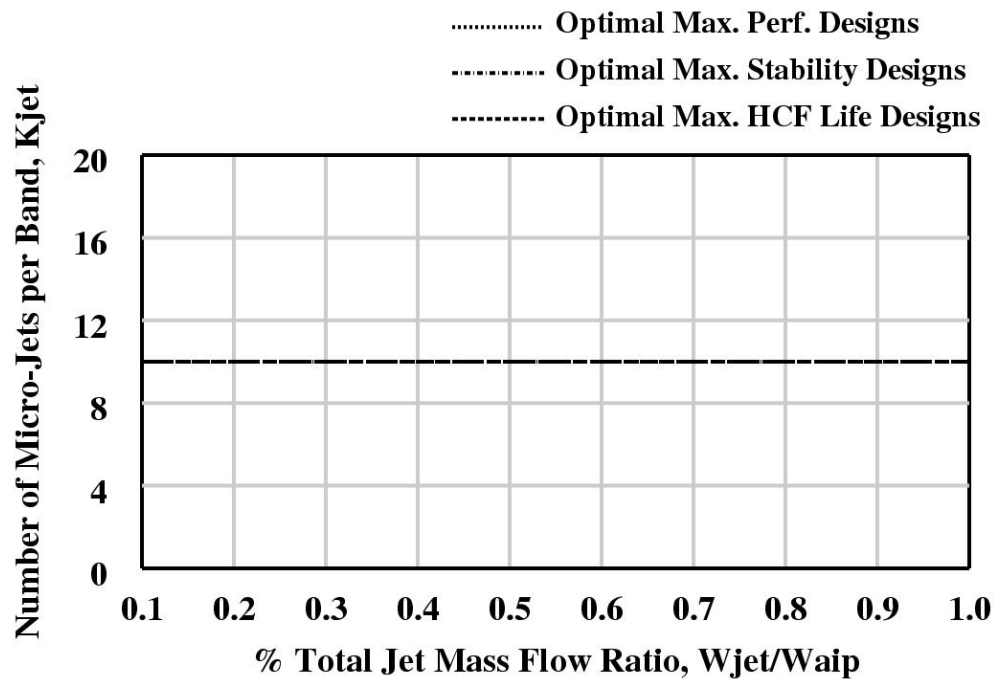
Figure (21): Effect of percent total jet mass flow ratio (Wjet/Waip on optimal number micro-jets per band settings.
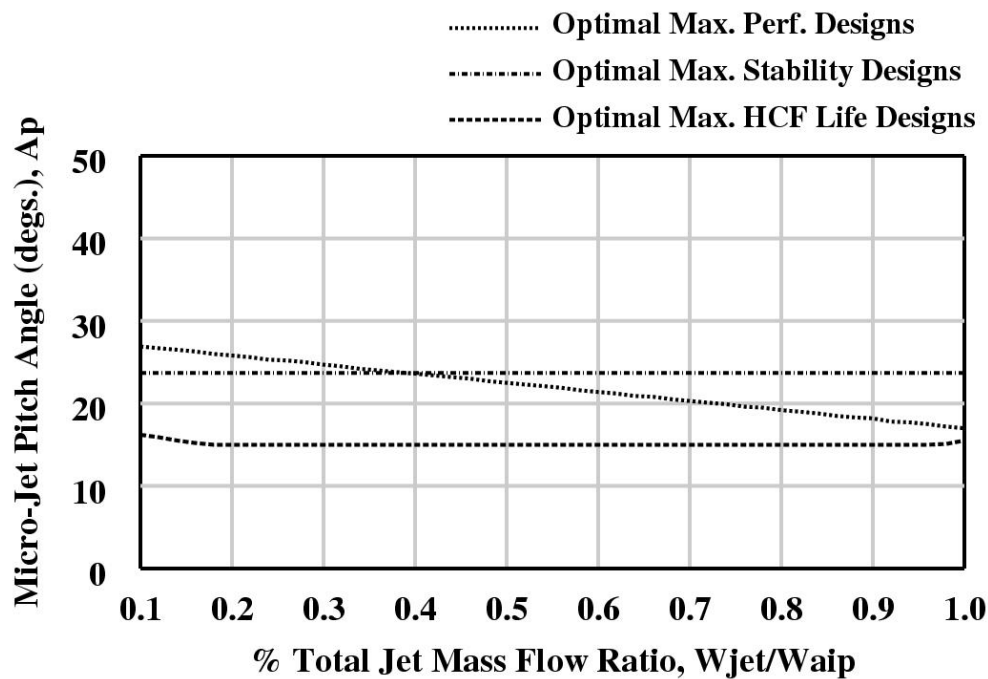
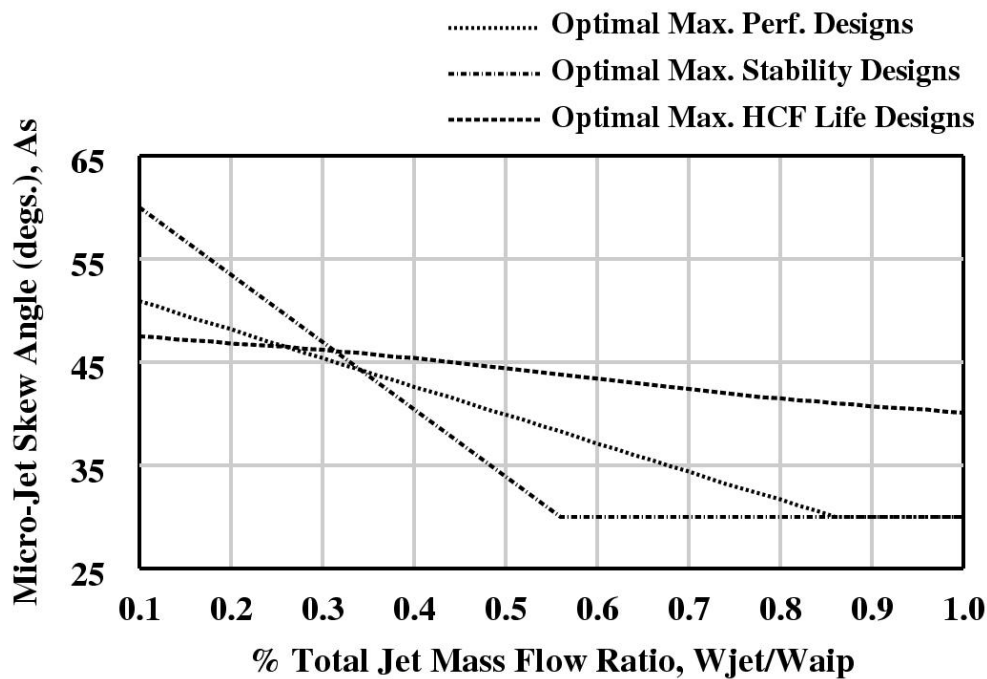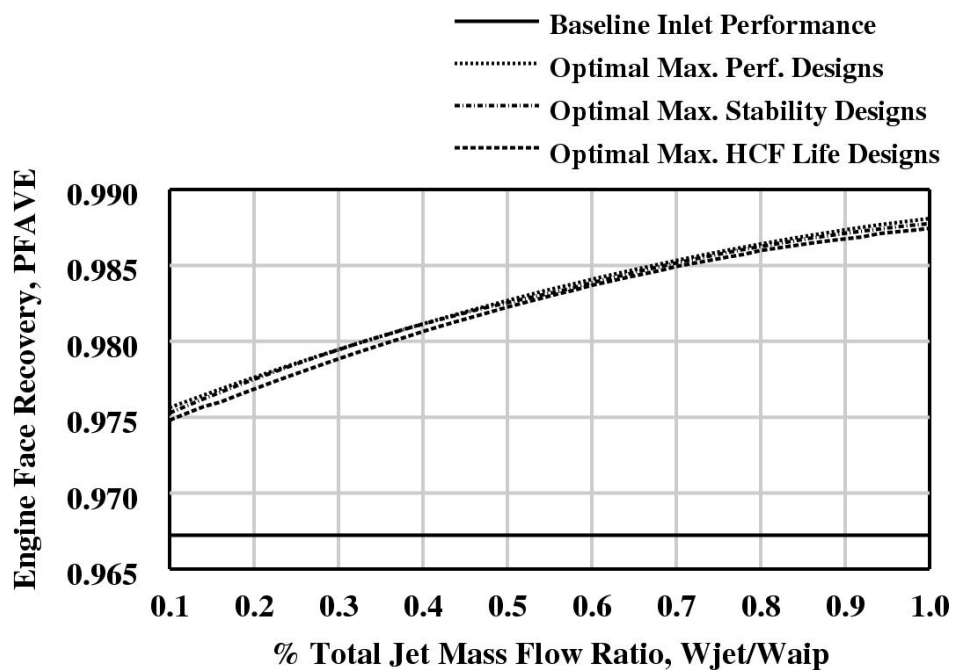**Figure (22): Effect of percent total jet mass flow ratio (Wjet/Waip) on optimal micro-jet pitch angle setting.**

Figure (23): Effect of percent total jet mass flow ratio (Wjet/Waip) on optimal micro-jet skew angle setting.

Figure (24): Effect of percent total jet mass flow ratio (Wjet/Waip) on inlet total pressure recovery, PFAVE.
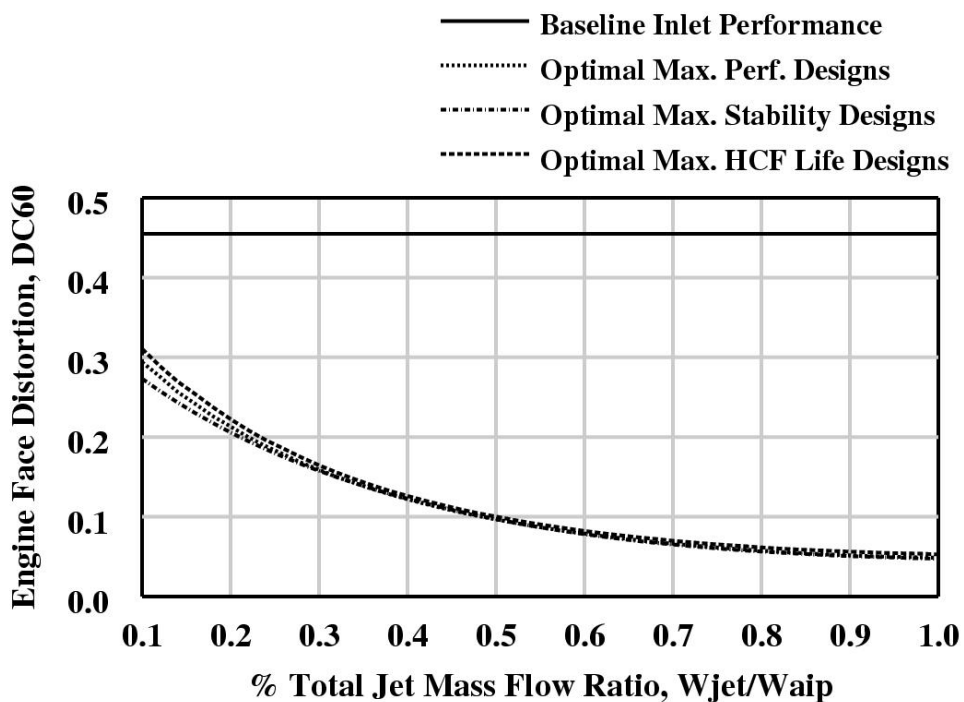
Figure (25): Effect of percent total jet mass flow ratio (Wjet/Waip) on engine face distortion, DC60.
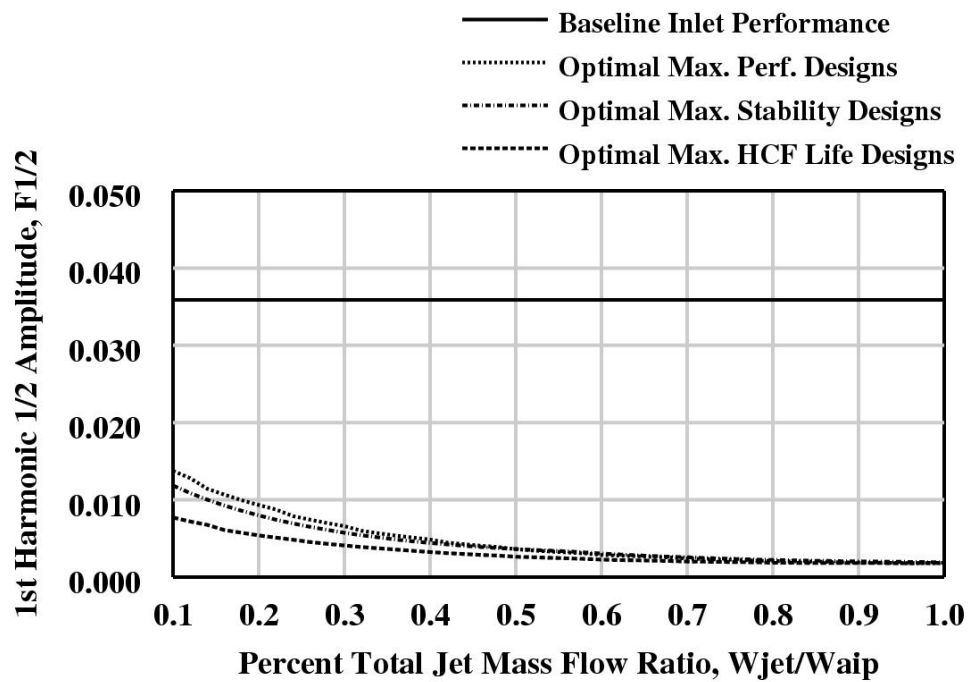
Figure (26): Effect of percent total jet mass flow ratio (Wjet/Waip) on 1st Fourier harmonic 1/2 amplitude, F1/2.
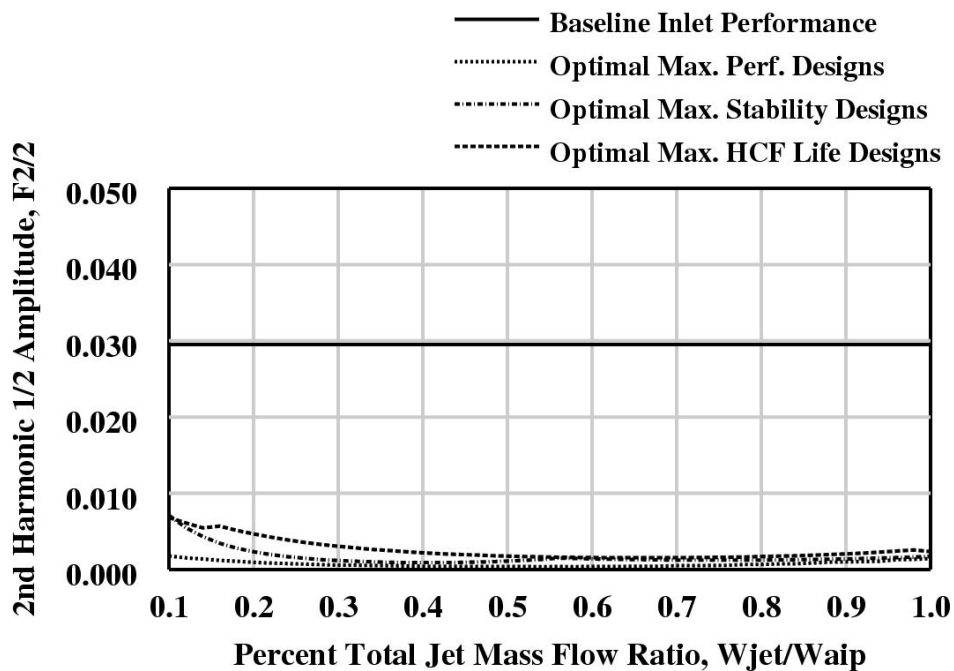
Figure (27): Effect of percent total jet mass flow ratio (Wjet/Waip) on 2nd Fourier harmonic 1/2 amplitude, F2/2.
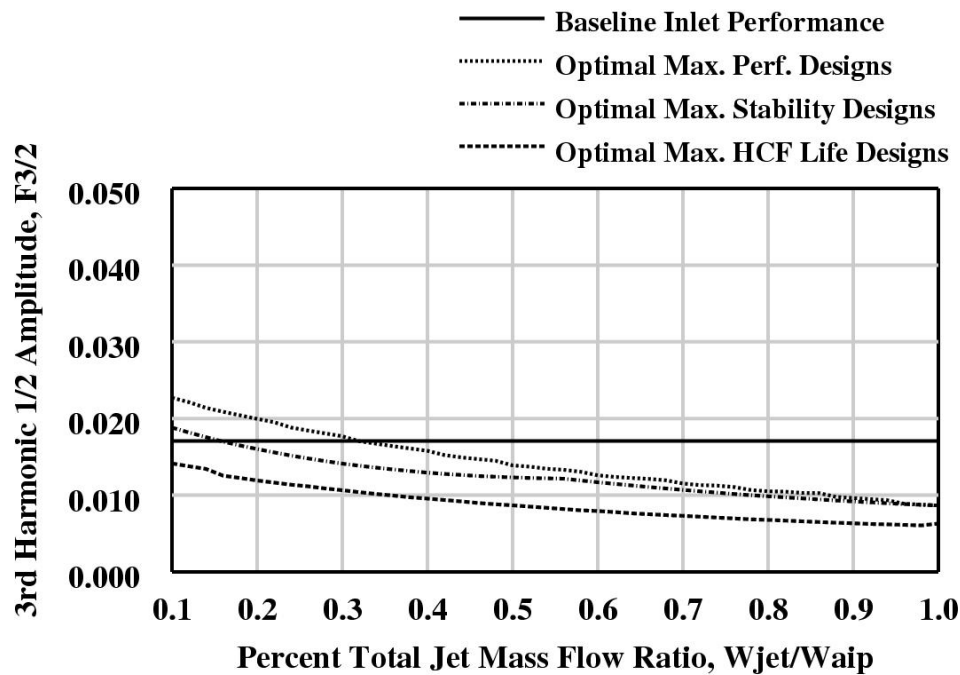
Figure (28): Effect of percent total jet mass flow ratio (Wjet/Waip) on 3rd Fourier harmonic 1/2 amplitude, F3/2.
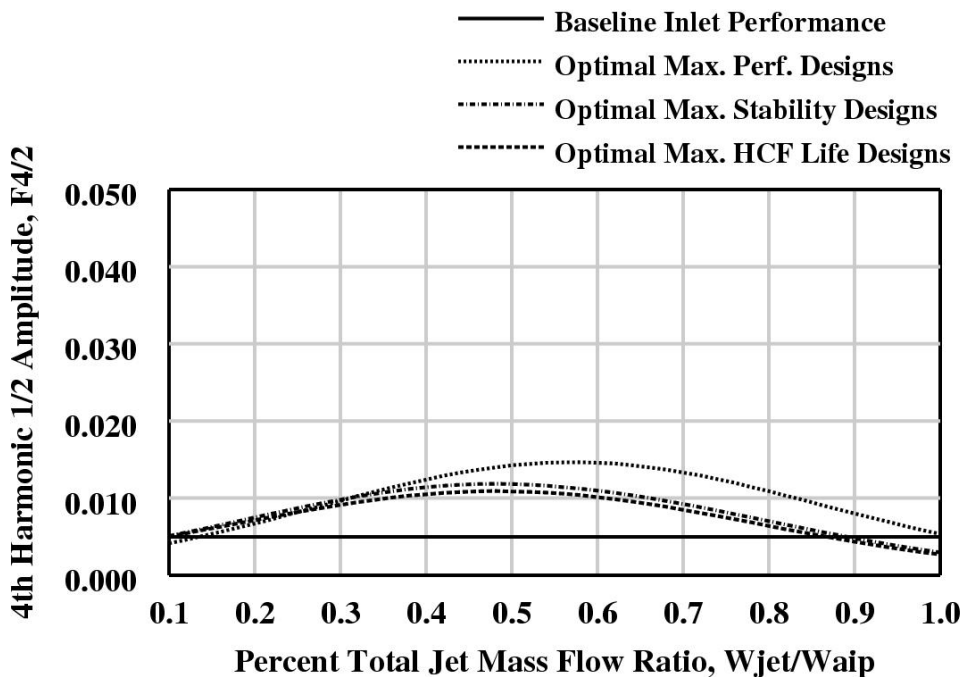
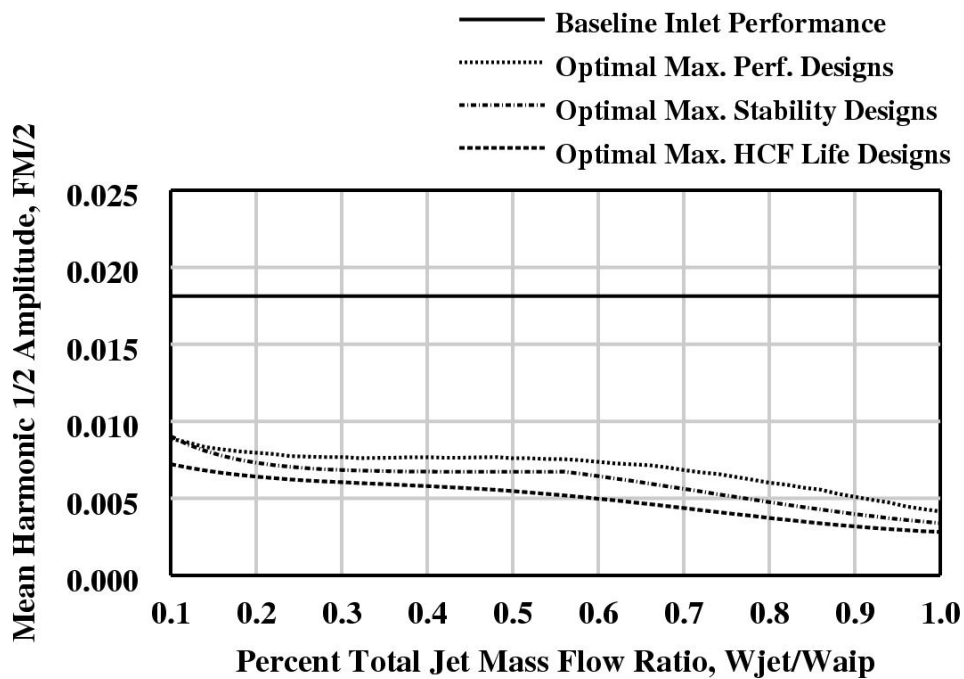**Figure (29): Effect of percent total jet mass flow ratio (Wjet/Waip) on 4th Fourier harmonic 1/2 amplitude, F4/2.**
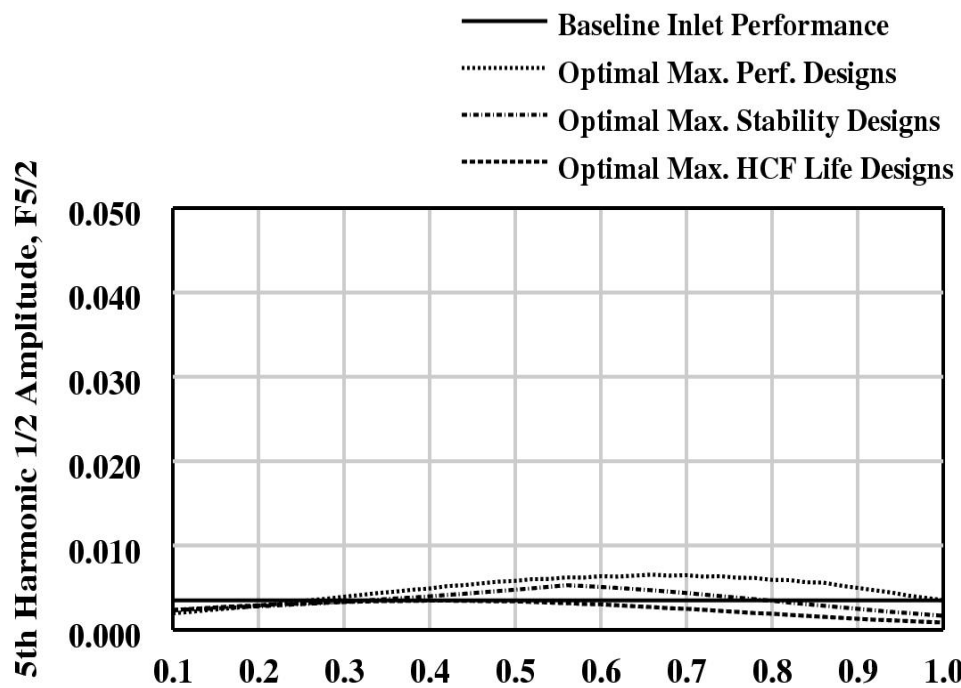
Figure (30): Effect of percent total jet mass flow ratio (Wjet/Waip) on 5th Fourier harmonic 1/2 amplitude, F5/2.

Figure (31): Effect of percent total jet mass flow ratio (Wjet/Waip) on the mean Fourier harmonic 1/2 amplitude, FM/2.

Config.	Grid	Kbnd	Kjet	Ap	As	% wjet/Waip
nvg201	81x91x49	1.0	10.0	15.0	30.0	0.1
nvg401	81x181x49					
nvg601	81x361x49					
nvg204	81x91x49	5.0	20.0	15.0	30.0	0.01
nvg604	81x181x49					
nvg504	81x361x49					
nvg208	81x91x49	5.0	20.0	45.0	30.0	0.001
nvg408	81x181x49					
nvg608	81x361x49					

Table (13): Conformation test cases for computational grid sensitivity study.

| Config.	PFAVE	DC(60)	F1/2	F2/2	F3/2	F4/2	F5/2
nvg201	0.98636	0.04713	0.00175	0.00394	0.00980	0.00416	0.00278
nvg401	0.98712	0.04698	0.00232	0.00191	0.00878	0.00110	0.00494
nvg601	0.98759	0.03227	0.00246	0.00406	0.00800	0.00307	0.00172
nvg204	0.98684	0.04823	0.00453	0.00926	0.00912	0.00099	0.00026
nvg404	0.98646	0.04889	0.00400	0.00985	0.00877	0.00096	0.00089
nvg604	0.98655	0.03090	0.00419	0.00713	0.00592	0.00051	0.00248
nvg208	0.97169	0.37704	0.03184	0.02786	0.01672	0.00478	0.00320
nvg408	0.97093	0.38311	0.03260	0.02824	0.01676	0.00449	0.00341
nvg608	0.97140	0.37298	0.03257	0.02799	0.01629	0.00406	0.00365

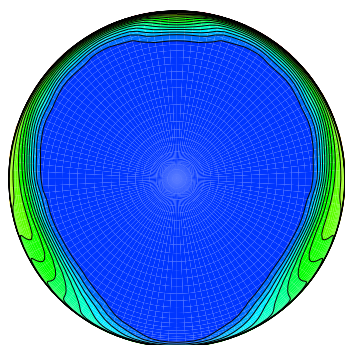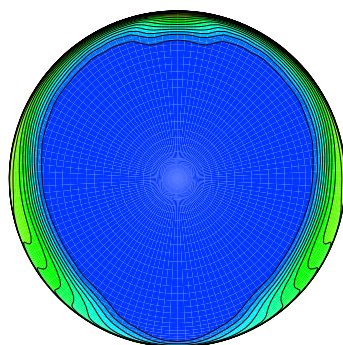**Table (14): Grid sensitivity study CFD engine face performance results.**
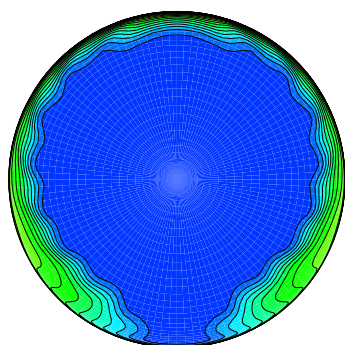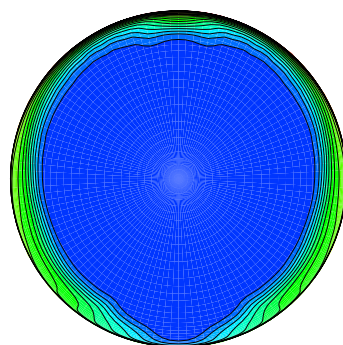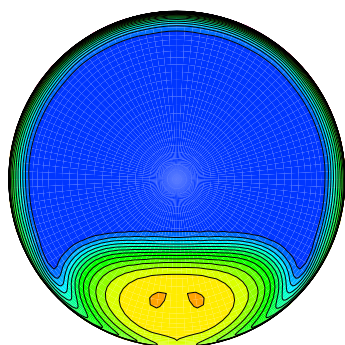
Config. nvg201
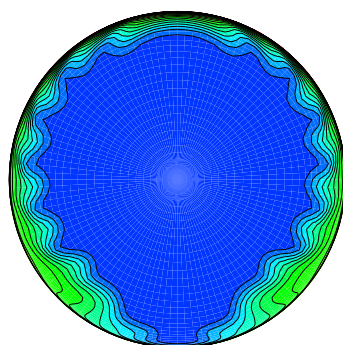
Config. nvg401
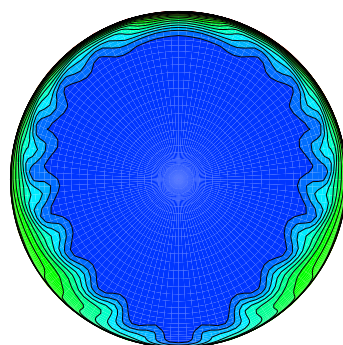
Config. nvg601

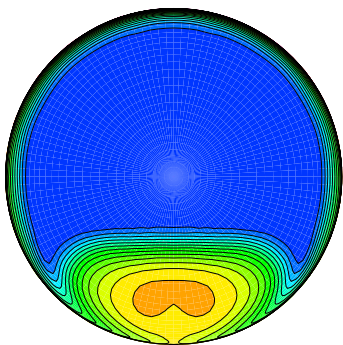**Config. nvg204**

Config. nvg404
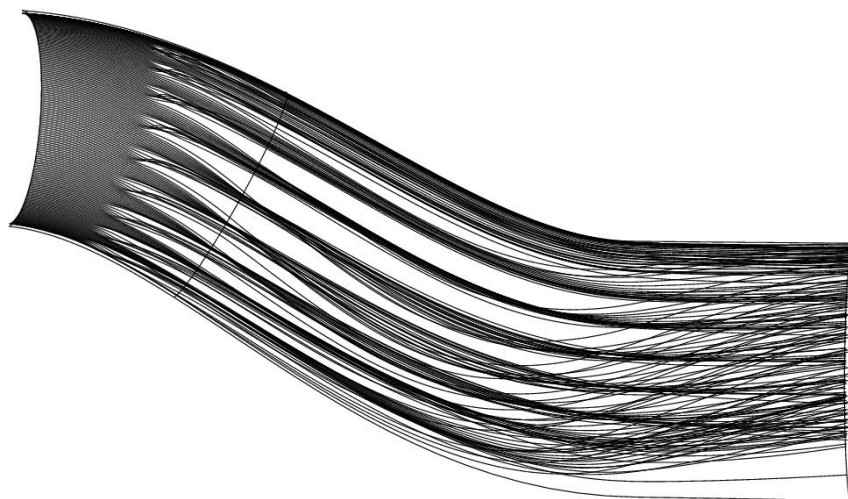
Config. nvg604

Config. nvg208
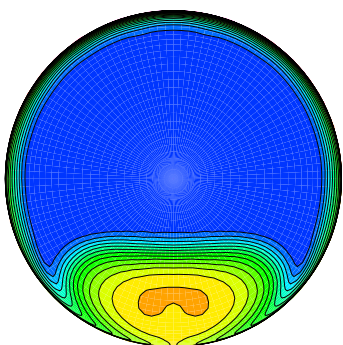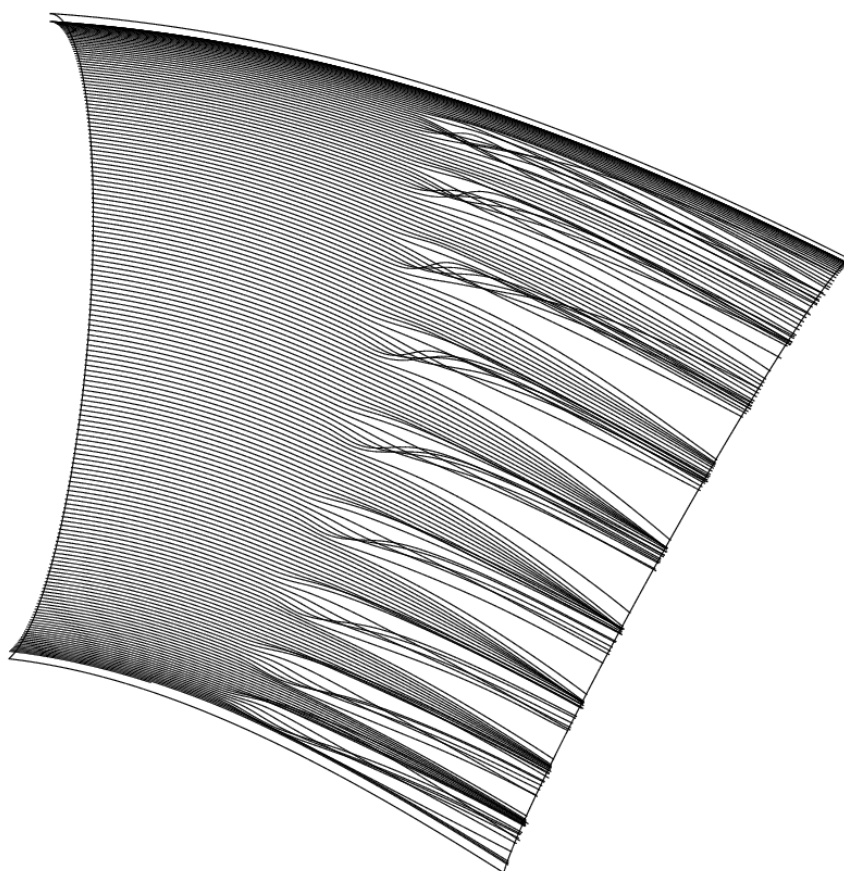
Config. nvg408

Config. nvg608

Figure (32): Engine face total pressure recovery contours for the computational grid sensitivity study.

(a) Inlet near wall streamlines.

(b) Effector region near wall streamlines.

Figure (33): Near wall streamlines for DOE micro-jet configuration nvg401, Kbnd = 1, Kjet = 10, Ap = 15.0 (degs), As = 30.0 (degs), Wjet/Waip = 1.0%, wjet/Waip = 0.100%.
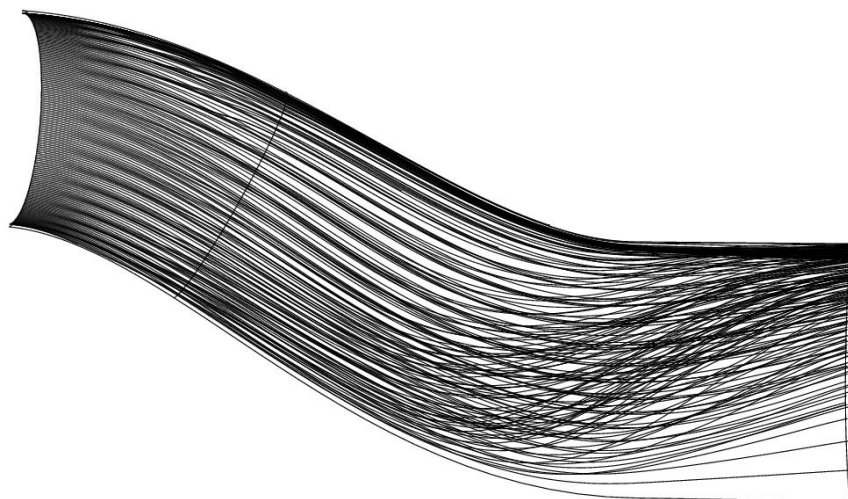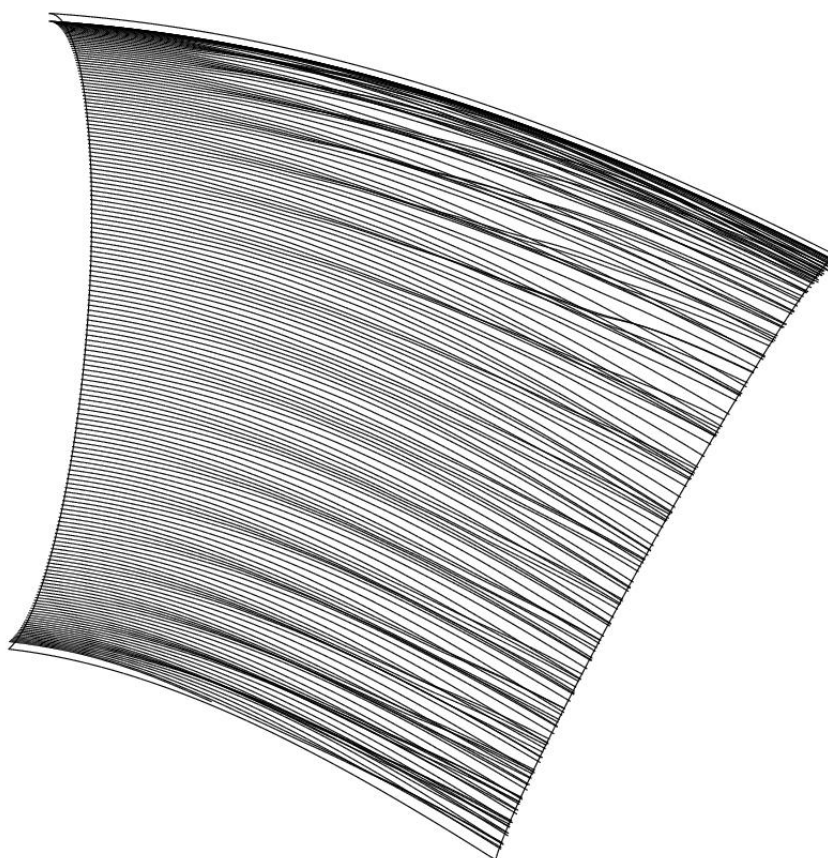
(a) Inlet near wall streamlines.

(b) Effector region near wall streamlines.

Figure (34): Near wall streamlines for DOE micro-jet configuration nvg404, Kbnd = 5, Kjet = 20, Ap = 15.0 (degs), As = 30.0 (degs), Wjet/Waip = 1.0%, wjet/Waip = 0.010%.
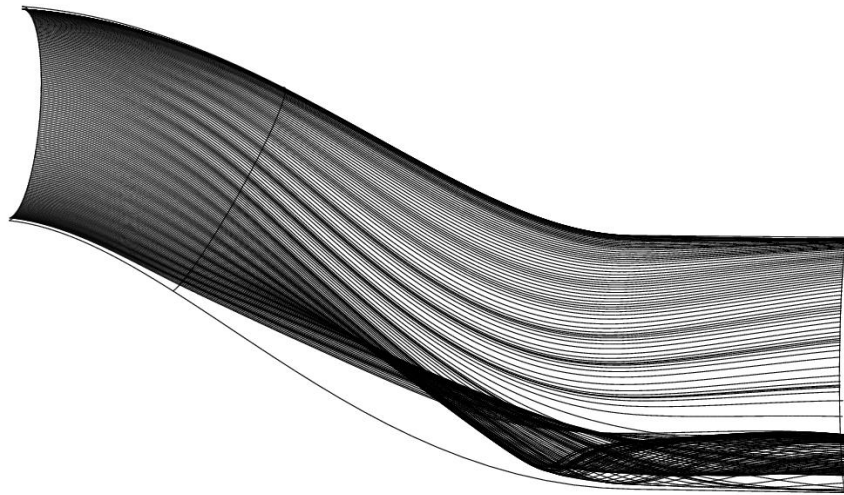
(a) Inlet near wall streamlines.

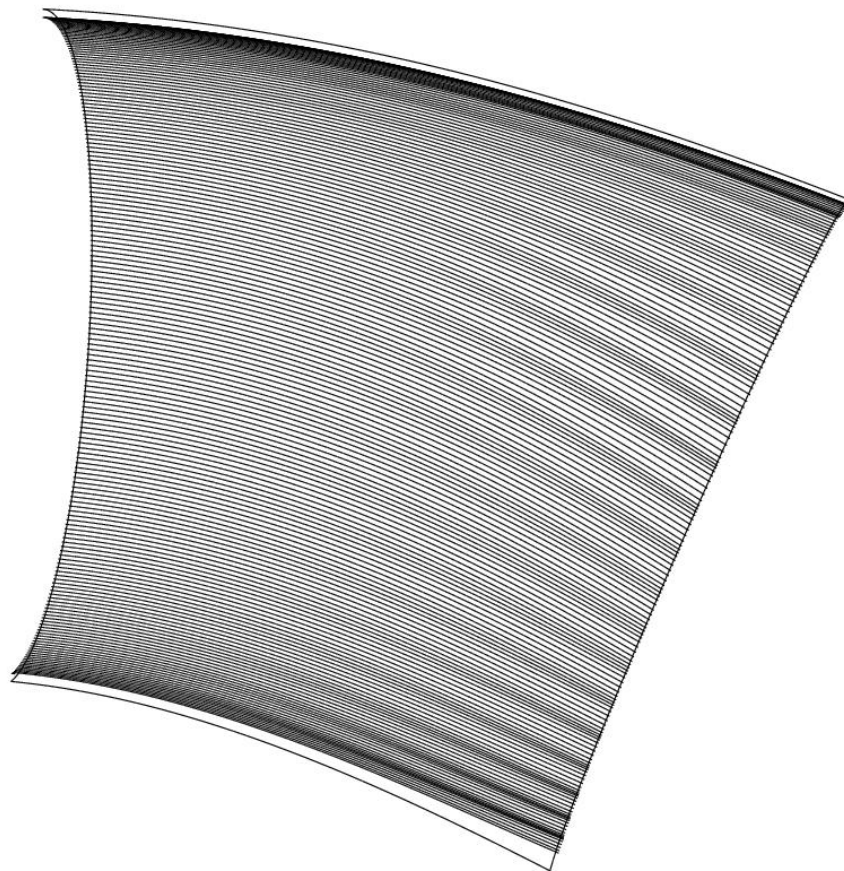**(b) Effector region near wall streamlines.**

Figure (35): Near wall streamlines for DOE micro-jet configuration nvg408, Kbnd = 5, Kjet = 20, Ap = 45.0 (degs), As = 30.0 (degs), Wjet/Waip = 0.10%, wjet/Waip = 0.001%.

Response	Config.	CFD	DOE	t	t*	Comments
PFAVE	nvg201	0.98636	0.98806	2.11991	1.70798	Not Diff.
DC60		0.04713	0.03939	2.02961	0.27203	Not Diff.
F1/2		0.00175	0.00172	1.96920	0.03898	Not Diff.
F2/2		0.00394	0.00188	1.96927	1.65680	Not Diff.
F3/2		0.00980	0.00795	1.96927	0.90716	Not Diff.
F4/2		0.00416	0.00531	1.96931	1.09997	Not Diff.
F5/2		0.00278	0.00340	1.96931	2.00063	Not Diff.
FM/2		0.00449	0.00459	1.96920	0.07475	Not Diff.
PFAVE	nvg204	0.98684	0.98672	2.11991	0.16519	Not Diff.
DC60		0.04823	0.03439	2.02961	0.13803	Not Diff.
F1/2		0.00453	0.00260	1.96920	1.25808	Not Diff.
F2/2		0.00926	0.01351	1.96927	0.74071	Not Diff.
F3/2		0.00912	0.00879	1.96927	0.16381	Not Diff.
F4/2		0.00099	0.00103	1.96931	0.15387	Not Diff.
F5/2		0.00026	0.000814	1.96931	0.76256	Not Diff.
FM/2		0.00483	0.00479	1.96920	0.02815	Not Diff.
PFAVE	nvg208	0.97169	0.97057	2.11991	1.13062	Not Diff.
DC60		0.37704	0.43563	2.02961	0.83884	Not Diff.
F1/2		0.03184	0.07767	1.96920	2.42600	Diff.
F2/2		0.02786	0.07811	1.96927	1.96150	Not Diff.
F3/2		0.01672	0.01446	1.96927	0.61218	Not Diff.
F4/2		0.00478	0.00530	1.96931	0.41032	Not Diff.
F5/2		0.00320	0.00348	1.96931	0.26311	Not Diff.
FM/2		0.01688	0.01919	1.96920	0.41672	Not Diff.

Table (15): Statistical comparison between the CFD analysis using the 89x91x49 grid and the DOE prediction from the regression model.

Response	Config.	CFD	DOE	t	t*	Comments
PFAVE	nvg601	0.98759	0.98806	2.11991	0.47221	Not Diff.
DC60		0.03227	0.03939	2.02961	0.18152	Not Diff.
F1/2		0.00246	0.00172	1.96920	0.80667	Not Diff.
F2/2		0.00406	0.00188	1.96927	1.72399	Not Diff.
F3/2		0.00800	0.00795	1.96927	0.02719	Not Diff.
F4/2		0.00307	0.00531	1.96931	2.46926	Diff.
F5/2		0.00172	0.00340	1.96931	216889	Diff.
FM/2		0.00386	0.00459	1.96920	0.58783	Not Diff.
PFAVE	nvg604	0.98655	0.98672	2.11991	0.23402	Not Diff.
DC60		0.03090	0.03439	2.02961	0.30528	Not Diff.
F1/2		0.00419	0.00260	1.96920	1.08129	Not Diff.
F2/2		0.00713	0.01351	1.96927	1.25329	Not Diff.
F3/2		0.00595	0.00879	1.96927	1.75693	Not Diff.
F4/2		0.00151	0.00103	1.96931	1.48613	Not Diff.
F5/2		0.00248	0.000814	1.96931	0.75090	Not Diff.
FM/2		0.00405	0.00479	1.96920	0.56806	Not Diff.
PFAVE	nvg608	0.97140	0.97057	2.11991	0.83787	Not Diff.
DC60		0.37298	0.43563	2.02961	0.90171	Not Diff.
F1/2		0.03257	0.07767	1.96920	1.50259	Not Diff.
F2/2		0.02799	0.07811	1.96927	1.95265	Not Diff.
F3/2		0.01629	0.01446	1.96927	0.73920	Not Diff.
F4/2		0.00406	0.00530	1.96931	1.05901	Not Diff.
F5/2		0.00365	0.00348	1.96931	0.14960	Not Diff.
FM/2		0.01691	0.01919	1.96920	0.41095	Not Diff.

Table (16): Statistical comparison between the CFD analysis using the 89x361x49 grid and the DOE prediction from the regression model.

REPORT DOCUMENTATION PAGE

1. AGENCY USE ONLY (Leave blank)	2. REPORT DATE	3. REPORT TYPE AND DATES COVERED
	February 2004	Technical Memorandum

4. TITLE AND SUBTITLE

Optimal Micro-Jet Flow Control for Compact Air Vehicle Inlets

5. FUNDING NUMBERS

WBS–22–708–92–24

6. AUTHOR(S)

Bernhard H. Anderson, Daniel N. Miller, Gregory A. Addington, and Johan Agrell

7. PERFORMING ORGANIZATION NAME(S) AND ADDRESS(ES)

National Aeronautics and Space Administration
John H. Glenn Research Center at Lewis Field
Cleveland, Ohio 44135–3191

8. PERFORMING ORGANIZATION REPORT NUMBER

E–14376

9. SPONSORING/MONITORING AGENCY NAME(S) AND ADDRESS(ES)

National Aeronautics and Space Administration
Washington, DC 20546–0001

10. SPONSORING/MONITORING AGENCY REPORT NUMBER

NASA TM—2004-212937

11. SUPPLEMENTARY NOTES

Bernhard H. Anderson, NASA Glenn Research Center; Daniel N. Miller, Lockheed Martin Aerospace Company, Fort Worth, Texas 76101; Gregory A. Addington, Wright-Patterson Air Force Base, Dayton, Ohio 45433; and Johan Agrell, Swedish Defence Research Agency, Bromma, Sweden SE–17290. Responsible person, Bernhard H. Anderson, organization code 5850, 216–433–5822.

12a. DISTRIBUTION/AVAILABILITY STATEMENT

Unclassified - Unlimited
Subject Category: 07   Distribution: Nonstandard

Available electronically at http://gltrs.grc.nasa.gov

This publication is available from the NASA Center for AeroSpace Information, 301–621–0390.

12b. DISTRIBUTION CODE

13. ABSTRACT (Maximum 200 words)

The purpose of this study on micro-jet secondary flow control is to demonstrate the viability and economy of Response Surface Methodology (RSM) to optimally design micro-jet secondary flow control arrays, and to establish that the aeromechanical effects of engine face distortion can also be included in the design and optimization process. These statistical design concepts were used to investigate the design characteristics of "low mass" micro-jet array designs. The term "low mass" micro-jet may refers to fluidic jets with total (integrated) mass flow ratios between 0.10 and 1.0 percent of the engine face mass flow. Therefore, this report examines optimal micro-jet array designs for compact inlets through a Response Surface Methodology.

14. SUBJECT TERMS

Aeronautics; Propulsion; Fluid dynamics

15. NUMBER OF PAGES

64

16. PRICE CODE

17. SECURITY CLASSIFICATION OF REPORT	18. SECURITY CLASSIFICATION OF THIS PAGE	19. SECURITY CLASSIFICATION OF ABSTRACT	20. LIMITATION OF ABSTRACT
Unclassified	Unclassified	Unclassified	